Computer Simulations of Laser Ablation of Molecular Substrates

Leonid V. Zhigilei* and Elodie Leveugle

Department of Materials Science and Engineering, 116 Engineer's Way, University of Virginia, Charlottesville, Virginia 22904

Barbara J. Garrison, Yaroslava G. Yingling, and Michael I. Zeifman

Department of Chemistry, 152 Davey Laboratory, Penn State University, University Park, Pennsylvania 16802

Received June 5, 2002

Contents

I. Introduction

Laser ablation of molecular systems constitutes a basis for a diverse range of well-established applications, from matrix assisted laser desorption/ionization (MALDI) and other laser-driven techniques for mass spectrometric analysis of large nonvolatile biomolecules[1−3] to laser surgery[4] and to surface microfabrication and pulsed laser deposition (PLD) of organic films and coatings.[5,6] Emerging applications of laser ablation are expanding into new areas, such as nanotechnology and microfabrication of electronic devices,[7] restoration of painted artworks,[8,9] and the design of laser plasma thrusters for microsatellites.[10] Further optimization of experimental parameters in current applications and the emergence of new techniques based on laser ablation can be facilitated by a better theoretical understanding of the relation between the basic mechanisms of laser interaction with materials, nonequilibrium processes caused by the fast deposition of laser energy, and the resulting parameters of the ejected ablation plume and the state of remaining target.

To date, however, the pace of the development and commercialization of new applications of laser ablation has been much higher than the one of a more gradual progress in the mechanistic understanding of the laser ablation phenomenon. Most of the available experimental data have been generated as a side product of the development of practical applications and only certain parameters of laser ablation of direct relevant to optimization of existing technologies have been addressed. There is, however, a growing number of experimental studies that are specifically aimed at investigating the fundamental processes in laser ablation. In particular, systematic studies of the role of the laser pulse duration,[11−14] fluence and wavelength,[15−17] size of the laser spot,[15] number of successive laser pulses,[18] laser beam incidence angle,[19,20] initial temperature of the molecular substrate,[21] and molecular volatility[22] have been performed. In addition to the yields[11,15,16,21] and velocities[17,23−27] of the ejected molecules and ions, that are commonly measured in time-of-flight mass spectrometry experiments, other parameters, such as cluster ejection[28−30] and profiles of the acoustic signals propagating from the ablation region[31−39] have been investigated, providing a more complete picture of the ablation process. Time-resolved spectroscopy and imaging methods have been also employed to study the dynamics of material disintegration and the ablation plume expansion.[40−42]

The growing experimental effort has been supported by theoretical studies,[3,43−47] numerical analysis of kinetic models,[48−53] and molecular dynamics (MD) simulations of laser desorption/ablation.[54−78] The diversity and complexity of the intertwined processes involved in laser ablation and occurring at different time and length scales present a challenge for theoretical and computational descriptions of this

* Corresponding author, E-mail: lz2n@virginia.edu.

10.1021/cr010459r CCC: $44.00
Published on Web 01/15/2003

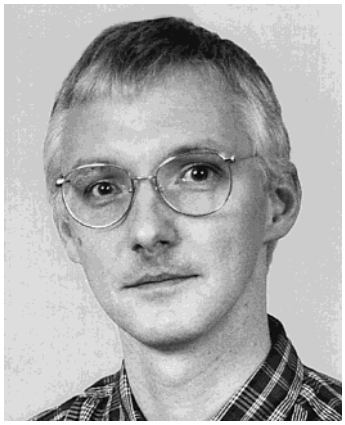

Leonid V. Zhigilei was born in Vilnius, Lithuania, studied materials science and metallurgy at the Leningrad Polytechnic Institute (at present St. Petersburg State Technical University), Russia, and received his University Diploma in 1987. His Ph.D. dissertation work on the structure of metallic glasses was performed at Tomsk State University and St. Petersburg State University, Russia (Ph.D. degree 1991). After several years of industrial work in Russia and Lithuania and a postdoctoral work in the Department of Chemistry at the Pennsylvania State University, in 2000 he joined the Department of Materials Science and Engineering at the University of Virginia as an Assistant Professor. His research interests are in the area of computational materials science and include the development of multiscale computational methods, investigation of laser-materials interactions, structure and properties of noncrystalline and nanostructured materials.

Elodie Leveugle was born in Paris, France, studied chemistry at the National Graduate School of Chemistry of Lille, France, and is currently a graduate student in Materials Science at the University of Virginia under the guidance of Leonid V. Zhigilei. Her Master dissertation is on the mechanisms of laser ablation of organic and polymeric materials.

Barbara J. Garrison was born in Big Rapids, Michigan, and studied physics at Arizona State University and theoretical chemistry at the University of California at Berkeley, receiving her Ph.D. in 1975. She held a postdoctoral position at Purdue University and a Lecturer position at UC Berkeley before joining the chemistry faculty at Penn State University in 1979 where she is currently Shapiro Professor of Chemistry. Her research interests include fast energy deposition processes at surfaces as related to mass spectrometry as in the techniques of secondary ion and matrix assisted laser desorption ionization mass spectrometries. Services activities include Chair of the New Chemistry Building Committee at Penn State and Vice-Chair Elect of the Division of Physical Chemistry of the American Chemical Society.

Yaroslava G. Yingling was born in Leningrad (now St. Petersburg), Russia, studied computer science and engineering at the Leningrad Polytechnic Institute (at present St. Petersburg State Technical University), Russia, and received her University Diploma in 1996. She is currently a graduate student in Materials at Penn State University under the guidance of Barbara J. Garrison. Her Ph.D. dissertation work is on the photochemical processes in laser ablation.

phenomenon. The processes include primary elementary excitations of optically active states in a molecular solid, thermalization of the deposited laser energy, formation of a highly energetic high-temperature and high-pressure region, explosive disintegration and prompt forward ejection of a volume of material, intensive processes in the ejected plume, recondensation or deposition of the ejected particles in PLD, and propagation of a pressure wave into the bulk of the target away from the ablation region. It is difficult to provide a consistent analytical description of all the involved processes or to address all the relevant physics and chemistry within a single computational model.

To address different processes involved in laser ablation with appropriate resolutions and, at the same time, to account for the interrelations among the processes, a computational approach that combines different methods within a single multiscale model should be developed. One of the promising approaches to modeling of the laser ablation phenomenon is to build a multiscale computational model around the MD technique. The advantage of the MD method is that only details of the microscopic interactions need to be specified and no assumptions are made about the character of the processes under study. Moreover, the MD method is capable of providing a complete microscopic description of the dynamical processes involved in laser ablation. The challenges in application of the MD method for simulation of laser ablation, however, are the severe limitations of time and length scales. The limitations make it impossible to directly address certain aspects of laser ablation (e.g., long-term expansion of the

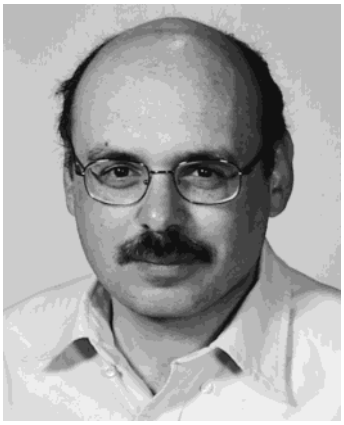

Michael I. Zeifman studied materials science and metallurgy at the Leningrad Polytechnic Institute (at present St. Petersburg State Technical University), Russia, and received his University Diploma in 1987. After years of industrial research, he returned to school in 1994 and received his M.Sc. degree in applied statistics (Technion, 1997) and Ph.D. in physical reliability (Technion, 2000). Currently, he is a postdoctoral researcher in Prof. Garrison's group at Penn State University. His research interests concentrate on application of statistical methods in mechanics and materials science.

ablation plume or propagation of the laser-induced pressure waves) in a MD simulation and dictate the necessity for combining the MD method with other computational techniques.

In the present paper, we review recent results of MD simulations of laser ablation of organic systems, highlight the advantages and limitations of the MD technique, and discuss the possibilities for integration of the MD method into a multiscale computational model capable of addressing a diverse range of physical and chemical processes involved in the laser ablation phenomenon. A general description of the multiscale model for laser ablation, as well as a more detailed discussion of the constituents of the model and recent computational developments is given next in Section II. A molecular-level picture of the laser ablation phenomenon, obtained from MD simulations, is presented for different irradiation conditions and related to experimental data and the existing theoretical models in Section III. The dynamics of the early stages of the ablation plume formation, the abundance of clusters and their distribution in the ejected plume, velocities of clusters and monomers, and other parameters of the ablation plume are discussed in Section IV. The profiles of the acoustic waves propagating from the absorption region are presented and related to the ablation mechanisms and experimental piezoelectric measurements in Section V. First results from a combined MD−direct simulation Monte Carlo (DSMC) simulation study of the ablation plume evolution are presented in Section VI. An overall picture of laser ablation of molecular systems emerging from the simulations is reviewed in Section VII.

II. Computational Methods for Laser Ablation of Molecular Systems

There is a great disparity in time- and length-scales among the different processes involved into laser ablation of molecular systems, from molecular excitation by photon absorption and subsequent energy redistribution (picoseconds), to disintegration and ejection of a surface region of the irradiated target (nanoseconds), and to the relatively slow evolution of the ejected plume (microseconds). The multiscale character of the involved processes makes it impossible to provide an adequate description of the laser ablation phenomenon within a single computational model, and a multiscale model combining a number of computational methods should be developed. A hierarchy of the computational methods and interconnections among the methods used in the multiscale model discussed in the present paper is schematically illustrated in Figure 1. Part A represents atomic-level simulations that can be used to study the channels and rates of the vibrational relaxation of excited molecules and the redistribution of the deposited energy between the translational and internal degrees of freedom of molecules,[56−60] as discussed in Section II.A. The information on the rates of the conversion of the internal energy of the excited molecules to the translational and internal motion of the other molecules can be verified in pump−probe experiments[79−81] and can be used for parametrization of the coarse-grained breathing sphere model designed for large-scale MD simulations of laser ablation,[61,64] part B of Figure 1. The breathing sphere model, briefly outlined in Section II.B, has been recently extended to include a description of photochemical processes.[72,73] This extension, that includes photochemical reactions leading to the formation of radicals and subsequent abstraction and

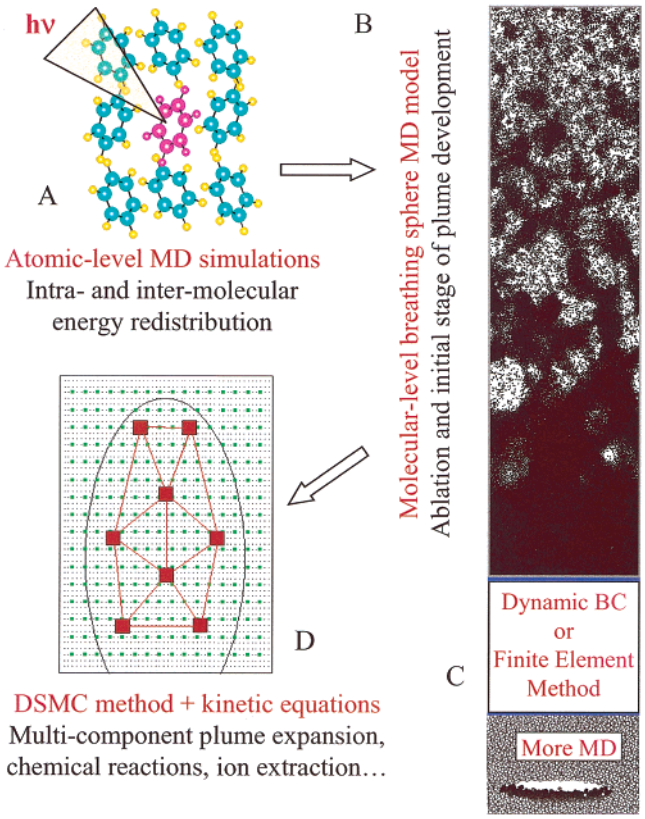

Figure 1. Schematic representation of the hierarchy of computational methods used to simulate processes involved in laser ablation of molecular materials with different resolution.[74]

recombination reactions, is discussed in Section II.C.

One effect that cannot be directly simulated within the breathing sphere model is the propagation of the laser-induced pressure waves from the absorption region deeper into the bulk of the irradiated sample. Even for the largest computational cell of 200 nm in depth used in the simulations, the wave reaches the back surface of the substrate at ~20 ps, whereas the ablation process takes hundreds of picoseconds. The wave reflected from the back surface can cause the effect known as back spallation,[82−84] when the tensile strength of the material is exceeded and fracturing occurs at a certain depth near the back surface of the sample, as schematically illustrated in part C of Figure 1. The reflected wave can also reach the front surface of the irradiated sample and contribute to the material ejection. Two approaches developed to avoid artifacts due to the pressure wave reflection, the dynamic boundary condition[83] and a combined MD−finite element method (FEM) technique,[85] part C of Figure 1, are reviewed in Section II.D.

The plume development in an MD simulation, part B of Figure 1, can be followed up to a few nanoseconds only, whereas the real time-scales of the plume expansion relevant to MALDI or PLD experiments are in the range of microseconds.[40,42] The long-term plume expansion can be simulated by the DSMC method, part D in Figure 1, whereas the initial conditions for DSMC simulation can be provided by the MD breathing sphere model simulations.[74,77,78,86,87] A fine grid of small black points in part D of Figure 1 schematically represents the spatial resolution in the DSMC model, as discussed in Section II.E. The kinetics of chemical reactions, cluster evaporation/growth, and ionization can be reproduced by solving a system of rate equations (shown schematically by green squares in part D of Figure 1). The results of the MD and DSMC simulations can be used to introduce dependences of the parameters of the rate equations on the local characteristics of the expanding plume. The rate equations, in return, provide information on the changes in the relative fractions of plume components (monomers, clusters, positive and negative ions, electrons) for DSMC calculations. The coarse grid and the squares shown in red in part D of Figure 1 represent MD simulations of cluster−cluster and cluster−monomer collisions that can be subsequently incorporated into DSMC simulation. A brief description of the computational techniques included into the multiscale model illustrated in Figure 1 and the connections among different components of the model is given below.

A. Atomic-Level Simulations

The atomic-level MD simulations have been used to study a range of processes involved in laser ablation.[56−60] One of the strengths of the atomistic simulations is the ability to provide detailed information on the rates and channels of energy redistribution among the translational, rotational, and internal degrees of freedom of molecules. In the case in which some of the molecules are excited by photon absorption, the rate of the energy transfer from the internal energy of the excited molecules to the thermal energy of a molecular solid is an important parameter that in a big part defines the character of the molecular ejection process.

A series of MD simulations of the vibrational energy redistribution during vibrational cooling and heating of a molecule in a molecular crystal have been performed by Kim et al.[88−90] The simulations have provided a detailed picture of the vibrational energy flow through various vibrational modes of the molecular system as well as information on the overall rates of vibrational cooling and heating. The direct application of the results of these calculations to the laser ablation phenomenon, however, is not possible. The vibrational cooling in a molecular crystal was simulated in these works for a single excited molecule under fixed external conditions (fixed density of the computational cell and fixed temperature of the surroundings). The energy transfer in laser ablation can be strongly affected by a relatively high density of excited molecules as well as complex dynamic conditions realized during the collective material ejection.

The vibrational to translational energy transfer under conditions of high excitation energy densities, when all the molecules are vibrationally excited at the beginning of simulation, has been analyzed for an oxygen crystal.[59] The anharmonic nature of the interatomic potential, the energy density created by the excitation, as well as the lattice structure and melting transition have been identified as the main factors determining the rate of the internal to translational energy transfer. When the energy deposition into an O_2 crystal was simulated in the presence of a free surface, molecular ejection was observed. At low excitation density, the ejection took form of a molecule-by-molecule desorption process, whereas at high excitation densities a forwarded ejection of a big part of the excited region was observed, as shown in Figure 2a. A similar picture of molecular ejection was observed in a simulation of fast heating of a nicotinic acid crystal containing a leucine enkephalin molecule,[58] Figure 2b. Following a temperature jump to 1500 K, almost all nicotinic acid molecules take off in this simulation, entraining and lifting up the leucine enkephalin molecule as well. In addition to the dynamics of intermolecular redistribution of the deposited energy, the atomic-level simulations also provide information on the conformational changes of the guest molecule undergoing laser desorption.[58,60]

A substrate-assisted method of laser energy deposition into a transparent molecular system, used in laser desorption mass spectrometry[91−95] and steam laser cleaning of surfaces,[96−98] has been explored in recent MD simulations by Dou et al.[99,100] In these simulations, molecular-level processes leading to the separation of a water film from a gold substrate quickly heated to 1000 K, are investigated. The fast heating of the metal surface mimics the effect of short pulse laser irradiation. Energy transfer from the hot substrate to the water film leads to the overheating and explosive boiling of a region of the film adjacent to the metal surface. The explosive boiling provides an outward force that lifts up the water film and separates it from the substrate, Figure 2c. The

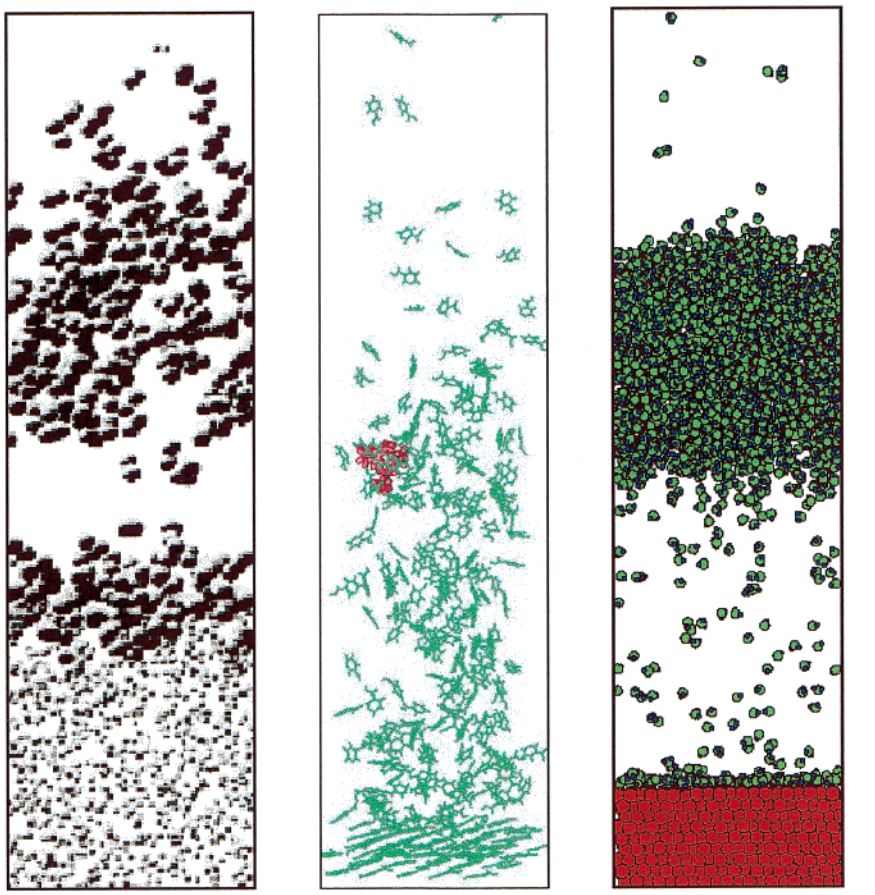

Figure 2. Snapshots from atomic-level simulations of laser ablation/desorption: (a) ejection of O_2 molecules from a γ-O_2 crystal sample due to the instantaneous deposition of 4 eV per molecule into the internal vibrational mode of each molecule in the upper half of the sample. Reprinted with permission from ref 59. Copyright 1999 American Chemical Society; (b) the ejection of a leucine enkephalin molecule embedded in a nicotinic acid crystal instantaneously heated to 1500 K. Reprinted with permission from ref 58. Copyright 1998 American Chemical Society; (c) substrate-assisted ejection of a water layer from a gold substrate heated to 1000 K. Reprinted with permission from ref 100. Copyright 2001 American Chemical Society. In (a) the snapshot is taken at 30 ps after the excitation, and the atoms are represented by spheres with radius proportional to their vibrational energy. In (b) the snapshot is taken at 10 ps after the instantaneous temperature jump, and most of the molecules that remain at the very bottom of the figure belong to a molecular layer that is kept rigid during the simulation. In (c) the snapshot is taken at 140 ps after the fast substrate heating, and the green, blue, and red spheres represent oxygen, hydrogen, and gold atoms, respectively.

thickness of the water film is found to have a strong effect on the character of molecular ejection. Faster cooling of the ejecta, more efficient volatilization, and higher ejection velocities observed for thin water films make them better candidates for mass spectrometry applications[91−95] as compared to the thick films.

Due to the high computational cost, the applicability of the atomic-level MD is limited to small systems and short simulation times, making it difficult to directly apply this technique for simulation of the whole ablation process, from laser irradiation to the collective molecular ejection. It is impossible, in particular, to reproduce a realistic laser energy deposition profile within a surface region of irradiated molecular target even for systems with highest absorption coefficients. A homogeneous energy deposition within a thin surface layer of the sample used in the simulations illustrated in Figure 2a,b and the proximity of the free (Figure 2a) or rigid (Figure 2b) boundary at the back of the computational cell can significantly affect the molecular ejection process and make it difficult to relate simulation results to real experimental conditions. In addition, the analysis of the ejected plume in terms of velocity, angular and cluster distributions requires a considerably bigger system and a longer simulation time so that statistically significant data can be obtained. To overcome the limitations of the atomic-level MD method, a new coarse-grained model for MD simulation of laser ablation of molecular solids has been developed.[61,64] This model, briefly described in the next section, is based on a molecular, rather than atomic-level, representation of a molecular solid and permits a significant expansion of the time and length-scales accessible for the simulations.

B. Mesoscopic Breathing Sphere model

In an atomic-level MD model a typical small molecule or a monomer unit can include tens of atoms and the time-step of integration of the equations of motion of 0.1 fs or smaller must be used to follow high-frequency vibrational motion of H, C, and N atoms. To overcome the limitations of the atomistic

MD model and to address collective processes leading to the material ejection in laser ablation, an alternative coarse-grained "breathing sphere" MD model has been developed.[61,64]

The breathing sphere model assumes that each molecule (or appropriate group of atoms) can be represented by a single particle. The parameters of interparticle interaction are chosen to reproduce the properties of the material, in this case, a molecular solid. In particular, the cohesive energy, vibrational/elastic properties, speed of sound, thermal conduction, melting and boiling temperatures, as well as strength and plasticity of the material are defined by the interparticle interaction potential. The equilibrium distance in the interparticle potential is defined as the distance between the edges of the spherical particles rather than their centers. This choice of equilibrium distance is based on the physical concept that the sublimation or cohesive energy of an organic solid is governed primarily by the interaction among atoms on the outside of the molecule and allows an easy means of simulating multicomponent molecular systems.[22,61,70,73,75,76,101]

To simulate molecular excitation by photon absorption and vibrational relaxation of the excited molecules, an additional internal degree of freedom is attributed to each molecule. This internal degree of freedom, or breathing mode, is realized by allowing the particles to change their sizes. The parameters of a potential function ascribed to the internal motion can be used to change the characteristic frequency of the breathing mode. The rate of the vibrational energy transfer is determined by the size of the anharmonicity of the potential function and frequency mismatch between the internal molecular motion and phonon modes in a molecular solid.[102−104] Thus, the parameters of the internal potential can be used to control the coupling between internal and translational molecular motions.[61] In effect, one can control the rate of the conversion of internal energy of the molecules excited by the laser to the translational and internal motion of the other molecules. The rate of the vibrational relaxation of excited molecules is an input parameter in the model and can be either estimated from experimental data[79−81] or modeled in atomistic[59,88−90] or ab initio[105] molecular dynamics simulations.

The laser irradiation is simulated by vibrational excitation of molecules that are randomly chosen during the laser pulse duration within the penetration depth appropriate for a given wavelength. Vibrational excitation is modeled by depositing a quantum of energy equal to the photon energy into the kinetic energy of internal motion of a given molecule. An alternative result of the photon absorption, photofragmentation of the excited molecule into fragments that can subsequently participate in chemical reactions, can be also reproduced within the model, as discussed in Section II.C. The total number of photons entering the model during the laser pulse is determined by the laser fluence, incident laser energy per unit surface area. The absorption probability can be modulated by Lambert−Beer's law to reproduce the exponential attenuation of the laser light with depth or can be restricted to a certain component within a complex material. The irradiation parameters and optical properties of the material are thus explicitly included in the model.

Since in the breathing sphere model each molecule is represented by a single particle, the system size can be sufficiently large to reproduce the collective dynamics leading to laser ablation and damage. Moreover, since explicit atomic vibrations are not followed, the time-step in the numerical integration of the equations of motion can be much longer and the dynamics in the irradiated sample can be followed for as long as nanoseconds. The limitations of the breathing sphere model are related to the approximation of all the internal degrees of freedom of a molecule by one internal mode. The rates of intermolecular energy transfer cannot be studied within the model, but have to be specified through the input parameters, as discussed above. A smaller number of degrees of freedom in the model system should also be taken into account when performing a quantitative comparison with experimental data, e.g., of the threshold fluence for the ablation onset.[67,69]

The system used in simulations described in Sections III−V is a generic molecular solid. The parameters of the intermolecular potential are chosen to represent the van der Waals interaction in a molecular solid with the cohesive energy of 0.6 eV, elastic bulk modulus of ∼5 GPa, and density of 1.2 g/cm^3. A mass of 100 Da is attributed to each molecule. An amorphous molecular solid prepared by melting of a close packed crystal and subsequent quenching from the melt[106] is used in the simulations. Depending on the research question addressed in the simulations, we use computational cells of different dimensions, $10 \times 10 \times 100$ nm (70 526 molecules), $10 \times 10 \times 180$ nm (126 950 molecules), $40 \times 10 \times 90$ nm (253 808 molecules), $40 \times 40 \times 90$ nm (1 015 072 molecules). Periodic boundary conditions are imposed in the directions parallel to the surface. These conditions simulate a situation in which the laser spot diameter is large compared to the penetration depth so that the effects of the edges of the laser beam can be neglected. At the bottom of the MD computational cell, we apply the dynamic boundary condition[83] developed to avoid artifacts due to reflection of the laser induced pressure wave from the boundary of the computational cell, as described in Section II.D. The laser irradiation at a wavelength of 337 nm (3.68 eV) and an absorption depth of 50 nm is used in most of the simulations. The absorption depth is in the range of the values characteristic of strongly absorbing molecular solids, e.g., some of the matrixes used in ultraviolet (UV)-MALDI.[107] The values of the laser pulse duration, 15 and 150 ps, are chosen to make sure that simulations are performed in two distinct irradiation regimes, stress confinement and thermal confinement, as discussed in Section III.E.2.

C. Photochemistry

To investigate the role of the photochemical processes in laser ablation, the breathing sphere model has been modified to allow the photon absorption event to break a chemical bond in the molecule.[72,73]

The excited molecule in this case breaks into radicals, which can subsequently undergo abstraction and recombination reactions. The reaction patterns in our model are based on photochemistry of chlorobenzene. The selection of chlorobenzene as the basic system for modeling photochemical events is based on the well-known photochemistry of the compound and extensive experimental studies[108−113] that make a detailed interpretation/verification of the simulation results possible. Photofragmentation of chlorobenzene occurs via scission of the C−Cl bond to yield C_6H_5 and Cl radicals, which in solution and static gas cell experiments react with each other and with the parent molecule to form a number of different products.[108−110,114]

To represent the photochemical processes in chlorobenzene, we chose reactions that are thermodynamically favorable and are observed in gas-phase or solution chemistry of chlorobenzene. In total, there are 12 reactions considered, a sample of which are delineated below.

Laser excitation of the molecule:

$$C_6H_5Cl + h\nu \rightarrow C_6H_5Cl^*$$

Photochemical fragmentation of the excited molecule:

$$C_6H_5Cl^* \rightarrow C_6H_5\bullet + \bullet Cl \qquad \Delta H^\circ_{rxn} = -79.5 \text{ kJ/mol}$$

Vibrational relaxation of the excited molecule:

$$C_6H_5Cl^* \rightarrow C_6H_5Cl \qquad \Delta H^\circ_{rxn} = -482.7 \text{ kJ/mol}$$

Abstraction reactions by primary radicals, for example:

$$C_6H_5Cl + \bullet Cl \rightarrow C_6H_4Cl\bullet + HCl$$
$$\Delta H^\circ_{rxn} = \text{from } -109.3 \text{ to } -66.4 \text{ kJ/mol}$$

Radical−radical recombination reactions, for example:

$$Cl\bullet + \bullet Cl \rightarrow Cl_2 \qquad \Delta H^\circ_{rxn} = -239.2 \text{ kJ/mol}$$

$$C_6H_5\bullet + \bullet C_6H_5 \rightarrow C_{12}H_{10}$$
$$\Delta H^\circ_{rxn} = -564.4 \text{ to } -478.9 \text{ kJ/mol}$$

For each reaction the standard heat of formation, ΔH°_{rxn}, is calculated from the available thermochemical data.[73] When any of these reactions occur, the corresponding ΔH°_{rxn} is the amount of energy (potential plus kinetic) deposited into the system. The amount of energy given off from each reaction depends on the phase state of the surroundings (solid, liquid, or gas) and is carefully monitored by adjusting initial positions of the reaction products and by performing additional local energy checks. All of the reactions considered are exothermic; thus, the addition of photochemistry into the system converts energy that has been stored in chemical bonds into energy available for inducing the ablation processes.

The details of the choice of the potential parameters for each of the species as well as protocol for determining when to allow the various reactions to occur is described elsewhere.[73] The prescription involves a probabilistic choice of reactions based on the local environment followed by conventional integration of the classical equations of motion. To perform simulations for a relatively large system of 126 950 molecules (10 × 10 × 191 nm), we use a multiple time step integration algorithm. The time step of 5 fs is used in the parts of the system where no reactions occur or no free radicals are present. In the regions where reactions are taking place, the time step is decreased to 0.5 fs.

D. Pressure Waves and Dynamic Boundary Condition

The generation of pressure waves is a natural result of the fast energy deposition in the case of short pulse laser irradiation.[31−39,69,71,83,115−117] For example, the formation and propagation of a plane pressure wave in a simulation of a molecular solid irradiated with a 15 ps laser pulse with fluence of 55 J/m^2 and penetration depth of 50 nm is shown in the form the pressure contour plots in Figure 3. The laser fluence in this case is above the ablation threshold fluence,[69] and a high compressive pressure builds up in the surface region of the irradiated target due to the thermoelastic stresses and ablation recoil. The initial thermoelastic pressure buildup occurring on the time scale of the laser pulse duration is noticeable in Figure 3a,b down to the depth of ∼140 nm. The pressure relaxes by driving a strong compression wave into the bulk of the sample, as shown by the solid arrow in Figure 3c. At the same time, the presence of the free surface near the high-pressure region leads to the development of the tensile component of the pressure wave that follows the compressive part in its propagation deeper into the bulk of the sample, as shown by the dashed arrow in Figure 3c. In agreement with predictions of analytical calculations,[115,116,118] the tensile component increases with depth and reaches its maximum at approximately one penetration depth beneath the surface, Figure 3c. The difference in slopes of the dashed and solid arrows in Figure 3 corresponds to the anticipated pressure dependence of the velocity of a pressure wave. The maximum value of the tensile component of the wave in this simulation is much lower than the maximum value of the compressive component of the pressure wave, which can be attributed to the contribution of the compressive ablation recoil pressure that partially cancels the tensile component, as well as inability of the material to support high tensile stresses, as discussed in more detail in Sections III.C and V.

To simulate propagation of the laser-induced pressure wave into the bulk of the sample, the size of the MD computational cell should be increased linearly with the time of the simulation. For times longer than a hundred picoseconds, the size of the model required to follow the wave propagation becomes computationally prohibitive. If large computational cells are not used, however, artificial border effects can interfere with the simulation results. Both rigid and free boundary conditions lead to the complete reflection of the pressure wave, as shown in Figure 3a,b. In the case of the free boundary condition, the compressive pressure wave transforms into the ten-

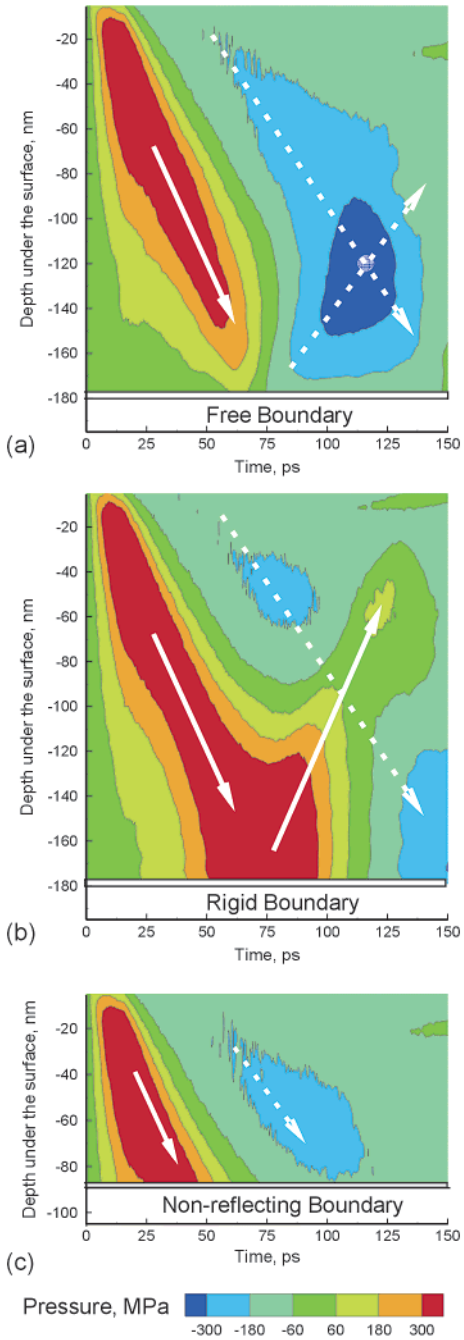

Figure 3. Pressure contour plots for MD simulations of 15 ps laser pulse irradiation of an organic target performed with (a) free boundary condition, (b) rigid boundary condition, and (c) the dynamic nonreflecting boundary condition[83] at the bottom of the MD computational cell. Larger computational cells of 180 nm in depth are used in the simulations with free and rigid boundary conditions, as compared to 10 × 10 × 90 nm computational cell used in the simulation with nonreflecting boundary. Solid and dashed arrows show the directions of the compressive and tensile waves propagation, respectively.

sile one upon reflection. The reflected tensile wave, superimposed with the tensile component of the original pressure wave propagating from the irradiated surface, can exceed the dynamic tensile strength of the material and cause fracturing (back spallation) at a certain depth near the back surface of the irradiated sample. The depth and time of the back spallation are marked in Figure 3a, and the microscopic picture of the spallation process is shown in part C of Figure 1. The reflected wave can also reach the front surface of the irradiated sample and contribute to the material ejection.

In the case of the rigid boundary condition, the amplitude of the compressive pressure wave doubles near the back surface and the wave reflects without changing its sign, Figure 3b. The reflected compressive wave superimposes with the tensile component of the original pressure wave at ~100 ps and reaches the front surface at ~170 ps. Interaction of the reflected compressive wave with the new surface formed as a result of laser ablation and weakened by the laser heating can cause additional front surface damage and can significantly contribute to the material ejection due to the front surface spallation. At the same time, the tensile component of the original pressure wave reaches the back surface and doubles its amplitude. The resulting concentration of the tensile stresses can be sufficient to separate the dynamic part of the computational cell from the rigid layer. Although the simulations with rigid boundary condition can be related to experiments performed for a thin absorbing organic layer deposited on a substrate,[23] in most cases we are interested in much larger systems for which the effect of the substrate can be neglected.

To avoid artifacts due to the pressure wave reflection, we developed a simple and computationally efficient boundary condition based on analytical evaluation of the forces acting on the molecules in the boundary region from the outer "infinite medium".[83] In this approach, the boundary condition is a set of terminating forces that are applied to the molecules in the boundary region. In the calculation of the terminating forces, that are updated at each integration time step, we take into account three effects, namely, the static forces that mimic interaction with molecules beyond the computational cell, the forces due to the direct laser energy absorption in and around the boundary region during the laser pulse, and the forces due to the pressure wave propagation through the boundary region. The contribution of the pressure wave to the terminating forces is calculated based on the traveling wave equation and is proportional to the instantaneous velocity of the boundary.

As shown in Figure 3c, the dynamic boundary condition allows one to simulate nonreflective propagation of the pressure wave through the boundary of the MD computational cell and to restrict area of the MD simulation to the region where active processes of laser-induced melting, ablation, and damage occur. Although a twice smaller, as compared to the simulations shown in Figure 3a,b, computational cell is used in the simulation performed with the nonreflecting boundary condition, no artifacts due to the pressure wave reflection are observed. The nonreflecting boundary conditions have been successfully used in simulations of laser ablation and damage of organic materials in which both planar[22,67−78,101] and spherical[119] pressure waves were generated. Recently, the boundary conditions have been also implemented and tested for metals.[120]

An alternative approach to the problem of pressure wave reflection is to combine the MD model with the continuum finite element method.[85,121] The advantage of this approach is the ability to study the long-range propagation of the waves and their interaction with other MD regions of a large system.[85] One possible effect of such interaction is back spallation, discussed above and schematically illustrated in part C of Figure 1.

E. Direct Simulation Monte Carlo Method for Simulation of the Plume Expansion

As important as the fast processes occurring during the first nanoseconds of MALDI are, they only set an initial stage for further slower processes in the ablation plume, Figure 4a. The processes occurring during the long-term plume expansion can include extensive collisions among the ejected molecules, clusters and ions, evaporation of clusters and cluster growth by condensation, ionization/neutralization and chemical reactions, and ion extraction by an external field. These processes, occurring on the time scale of microseconds, can lead to significant changes in the velocity and angular distributions of the ejected species and can have important implications for many applications of laser ablation, such as MALDI and PLD.

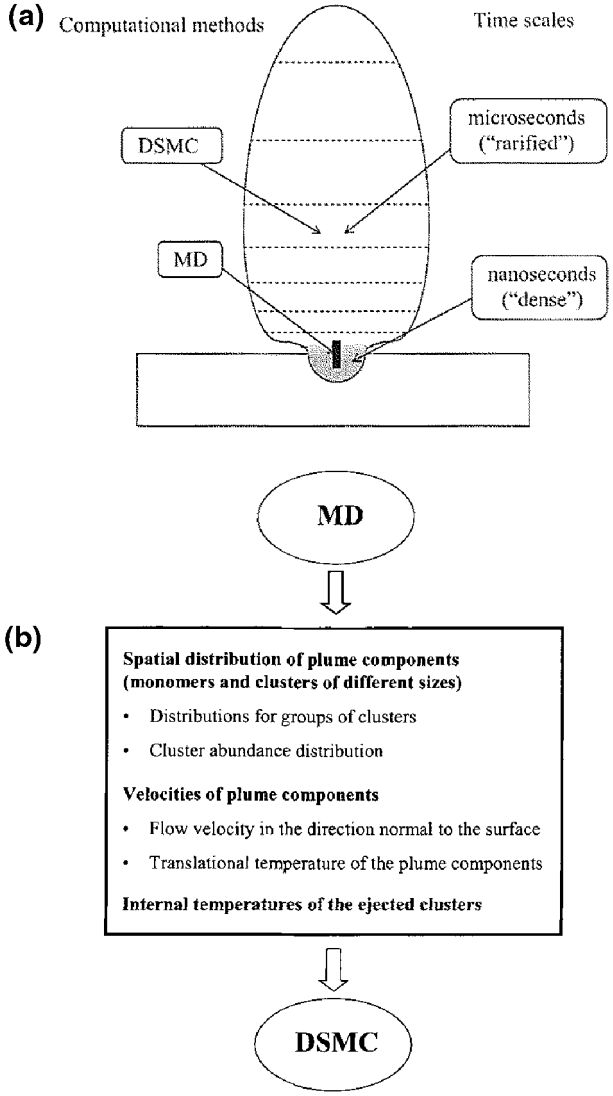

Figure 4. (a) Schematic illustration of a combined DSMC−MD computational method for simulation of laser ablation (MD) and long-term ablation plume expansion (DSMC). Parameters of the ablation plume needed for making connection between the MD and DSMC methods are listed in (b).

In addition to the long time-scales, the length-scale of the simulation should be increased to include an adequate description of the expansion of material ejected from the whole laser spot. While the expansion of the ablation plume in the lateral directions can be neglected during the first nanoseconds, and the periodic boundary conditions are appropriate for MD simulations, both lateral and axial expansions of the plume should be taken into account in the simulations of the long-term plume development. For a laser spot of 10−100 μm and an ablation depth of 10−100 nm, one can estimate that the number of molecules ejected from an irradiated molecular substrate in a single laser shot is in the range from tens of billions to trillions. These numbers are much beyond the limits of the MD simulation technique.

Among several alternative methods that can be considered for simulation of the long-term ablation plume expansion, part D in Figure 1, the direct simulation Monte Carlo (DSMC) method[122−128] appears to be the most suitable technique for neutral or weakly ionized ablation plumes. The continuum description, based on the finite element solution of the Navier−Stokes equations, is well suited for high-density collision-dominated flows but is not appropriate for the low densities realized in the rapidly expanding ablation plumes. Moreover, the DSMC has an advantage of providing direct information on the velocity, energy and angular distributions of the involved species, whereas the continuum approach requires the distribution functions as input. Traditional particle-in-cell (PIC) codes only treat ions and electrons; there is no chemistry or collisions, although collisions can be included by merging PIC with Monte Carlo collision calculations[129] or by using the Langevin equation to calculate the Coulomb collision term.[71,130] The PIC method assumes that particles do not interact with each other directly, but through the fields which they produce according to Maxwell's equations. In any formulation, the PIC model is not appropriate for treating weakly ionized gases with significant interactions between the ions and neutrals.

The DSMC method in its traditional form is widely used and is well documented in literature, e.g., in a classical book by Bird.[122] Briefly, the region of the flow (e.g., plume expansion in laser ablation) is divided into a number of cells with the cell size determined by the local mean free path. The flow field is reproduced using a large number of simulated particles (typically 10^6−10^7) that are characterized by coordinates, velocities, internal energies, species types (for example, radicals, ions, and clusters of different sizes) and weight factors. The weight factor defines the number of real particles that are represented by each simulated particle. The evolution of

the system of particles is split into collisionless streaming and collisions. At each time step, all the particles are moved as if they do not interact, according to their current velocities and the external forces, e.g., gravitation or electric field force acting on ionized species. After all the particles are moved, a given number of particles are selected for collisions. Collision pairs are selected at random from the same cell regardless of the positions of the particles. The probability of collision acceptance is defined by the relative velocities and the collision cross-sections of the particles. New velocities and internal energies are calculated as a result of each collision event. Reactions, other than two-particle collisions (e.g., three-body collisions, evaporation from clusters) can be incorporated at the interaction stage.

As shown schematically in Figures 1 and 4a, the initial conditions for DSMC can be provided by MD simulations. To make a connection between the MD simulation of laser ablation and the DSMC simulation of the ablation plume expansion, an appropriate description of the multicomponent (containing a large number of clusters of different sizes) ablation plume obtained by the end of the MD simulation has to be developed. The number of clusters of any given size observed in a MD simulation is not sufficient to provide a statistically adequate representation of the spatial distribution of clusters in the plume (except for the smallest clusters composed of up to 6−7 atoms/molecules).[74,78] One possible solution of this problem is to divide clusters into groups.[74,86,87] The range of cluster sizes that form a group can be chosen so that clusters in a group have similar velocity and spatial distributions in the plume. The characteristics that can provide a connection between MD and DSMC simulations in the multiscale model are summarized in Figure 4b. Besides the initial and boundary conditions, interactions among clusters should be addressed for the DSMC procedure. Most frequent reactions are collisions (either elastic or sticking) and evaporation of clusters. MD simulations can be used for the identification of possible reactions and for calculation of the reaction cross sections.[131−135] The first simulations performed with the combined MD-DSMC approach have demonstrated the ability of the method to provide insights into the complex processes occurring during the evolution of the ablation plume.[86,87] Some of the results obtained to date are presented in Section VI.

III. Mechanisms of Laser Ablation

The MD method allows one to perform a detailed analysis of the laser ablation process in which thermodynamic parameters of the system can be correlated with microscopic dynamics at the molecular level. This capability of the MD method to provide insights into the mechanisms of material ejection has been used in recent breathing sphere model simulations performed with different laser fluences, pulse widths, and temperatures of the initial sample. A mere visual inspection of snapshots from different simulations, Figure 5, reveals a strong dependence of the mechanisms of material ejection on the irradiation conditions. The diverse range of

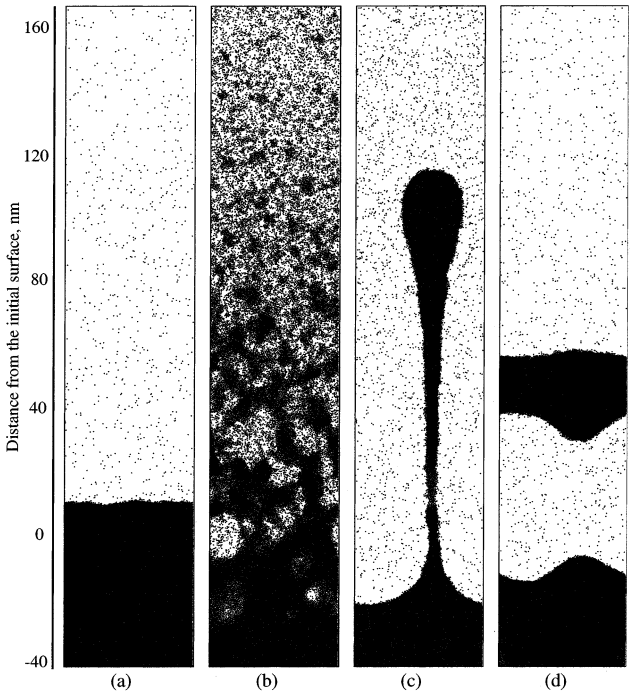

Figure 5. Snapshots from MD simulations of laser ablation of a molecular solid illustrating different mechanisms of material ejection: (a) desorption of monomers; (b) phase explosion of the overheated material; (c) hydrodynamic sputtering due to the fast melting and motion of liquid in the surface region; (d) photomechanical spallation of the surface layer caused by the relaxation of laser-induced thermoelastic stresses. The laser pulse durations are 150 ps (a, b) and 15 ps (c, d), fluences are 34 J/m^2 (a), 61 J/m^2 (b), 40 J/m^2 (c), and 31 J/m^2 (d). The laser penetration depth is 50 nm in all simulations. The irradiation parameters correspond to the regime of thermal confinement in (a) and (b) and to the regime of stress confinement in (c) and (d). The data are from ref 69 (Copyright 2000 American Institute of Physics) and ref 78 (Copyright 2003 Springer).

the observed processes includes molecule-by-molecule desorption from the irradiated surface at low laser fluences (Figure 5a), an explosive decomposition of an overheated surface region (Figure 5b), or formation of large droplets due to a transient melting and hydrodynamic motion of liquid in the surface region (Figure 5c) at higher laser fluences, as well as the ejection of large fractured solid fragments caused by photomechanical effects (Figure 5d). In this section, we perform a detailed analysis of the mechanisms of laser ablation/desorption revealed in the simulations.

A. Desorption

A typical snapshot from a simulation performed at low laser fluences is shown in Figure 5a. Mostly monomers are ejected from the surface heated by laser irradiation, suggesting that the thermal desorption model can provide an adequate description of molecular ejection process. Indeed, in the low fluence regime, the dependence of the yield of ejected molecules N on fluence F can be well described by an Arrhenius-type expression:[3,15,67−69]

$$N = A \exp\left[-\frac{E_s^*}{k_B(T_0 + BF)}\right] \quad \text{for } F < F_{th} \qquad (1)$$

where N is the number of molecules desorbed during the time of a simulation, E_s^* is an activation energy, A is a preexponential or frequency factor, B is a factor that describes the conversion of the deposited energy into an increase of temperature of the surface,[15,67] T_0 is the initial temperature of the molecular system, k_B is Boltzmann's constant, and F_{th} is a threshold fluence that defines the upper limit of validity of the desorption model. As we can see from the yield vs fluence dependences shown in Figure 6, eq 1 provides a good fit of the desorption yield with the same activation energy E_s^* of 0.46 eV for simulations performed with two different laser pulse durations, 150 and 15 ps, and two initial temperatures, 0 and 500 K. The preexponential factor A divided by the time of the simulation after the end of the laser pulse and the number of molecules at the surface of the computational cell is found to be of the same order as frequency of molecular vibrations, $\sim 10^{12}$ s^{-1}. The thermal desorption model thus provides an adequate description of the molecular ejection at low laser fluences.

At the lowest fluences at which a noticeable number of molecules is detected ($\sim$15 J/m^2 at $T_0 = 0$ K and $\sim$5 J/m^2 for $T_0 = 500$ K, the surface temperature reaches $\sim$735 K, a value slightly below the melting temperature of the model material, $\sim$750 K. At this fluence, the molecular ejection can be described as sublimation from a solid. As the fluence increases, the near surface region melts and evaporation from a liquid surface region occurs.[23,66]

B. Overheating and Phase Explosion

As can be seen in Figure 6, the total amount of the ejected material increases at a certain threshold fluence by more then an order of magnitude. For 150 ps pulses, the increase is from 579 molecules (0.8 nm layer of the original sample) at 34 J/m^2 to 8033 molecules (11.4 nm layer) at 37 J/m^2, Figure 6b. This stepwise transition from ejection of about a monolayer of molecules to a collective ejection, or ablation, of a significant part of the absorbing volume reflects qualitative changes in the ejection mechanism. The thermal desorption model is not valid in the ablation regime and a different analytical description of the yield vs fluence dependence should be used. We find that the amount of material ejected in the ablation regime can be relatively well described by a simple model in which the ablation depth follows the laser energy deposition and all material that absorbs an energy density higher than a critical energy density, E_v^*, is ablated.[67–69] With an exponential decay of laser intensity given by the Beer's law, the total number of molecules ejected per unit surface area is

$$N = n_m L_p \ln\left[\frac{F}{L_p(E_v^* - CT_0)}\right] \quad \text{for } F \geq F_{th}, \quad (2)$$

where L_p is the laser penetration depth, n_m is the molecular number density, and C is a specific heat capacity of the model material. Neglecting the temperature dependence of the heat capacity, CT_0 is the thermal energy density prior to laser irradiation. This expression predicts the existence of the threshold fluence $F_{th} = L_p(E_v^* - CT_0)$ at which the critical energy density E_v^* is reached in the surface layer. In the simulations performed with 150 ps laser pulse, i.e., in the regime of thermal confinement (see Section III.E.2), we find that the value of the critical energy

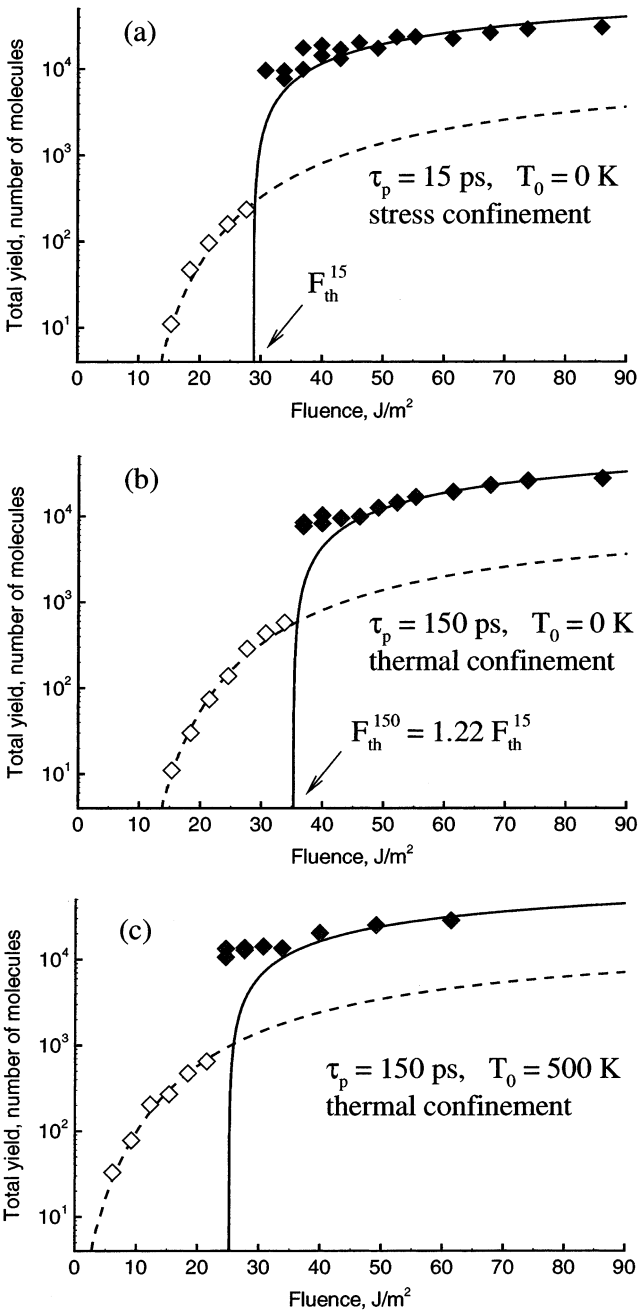

Figure 6. Total yield as function of laser fluence for simulations with two different initial temperatures of the sample, (a, b) $T_0 = 0$ K and (c) $T_0 = 500$ K and laser pulse durations of (a) 15 ps and (b, c) 150 ps. The open and closed symbols show the data points below and above the threshold for ablation. The solid lines represent prediction of the ablation model, eq 2, with (a) $E_v^* = 0.49$ eV and (b, c) $E_v^* = 0.6$ eV. The dashed lines represent fits of the data points below the threshold to the thermal desorption model, eq 1. The fits result in the same activation energy, $E_s^* = 0.46$ eV, for all three sets of the simulations. A logarithmic scale is used for better representation of low-fluence data. The data are from ref 68 (Copyright 1999 Springer) and ref 69 (Copyright 2000 American Institute of Physics).

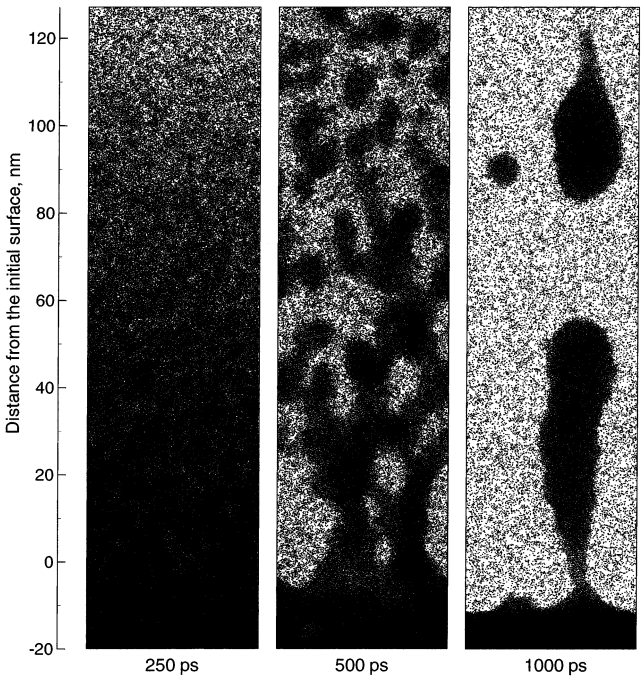

Figure 7. Snapshots from the simulation of laser ablation in the regime of thermal confinement. The laser pulse duration is 150 ps and fluence is 61 J/m^2 (1.75 times the ablation threshold fluence). The data are from ref 78 (Copyright 2003 Springer).

density obtained from the fit to the data points above the threshold fluence, Figure 6b, is equal to the cohesive energy of the model molecular solid, 0.6 eV. Expressions similar to the one given by eq 2 have been used to describe the fluence dependence of the ablation yield (or ablation depth) in photochemical laser ablation of polymers[32,48] and volume "layer-by-layer" molecular ejection in MALDI.[3,44]

Snapshots from a large scale simulation[78] performed with 40 × 40 × 90 nm (1 015 072 molecules) computational cell at laser fluence of 61 J/m^2, or 1.75 times the ablation threshold fluence, give a visual picture of the active processes occurring in the vicinity of the irradiated surface during the first nanosecond following the laser irradiation, Figure 7. In the first snapshot, shown for 250 ps, 100 ps after the end of the laser pulse, we see a homogeneous expansion of a significant part of the surface region. The homogeneous expansion is followed by the appearance of density fluctuations and gradual decomposition of the expanding plume into gas phase molecules and liquid phase regions. A closer view at a snapshot of a part of the ablation plume taken at a time of 200 ps, when the density fluctuations are apparent, is shown in Figure 8. The decomposition of the expanding plume leads to the formation of a foamy transient structure of interconnected liquid regions, as shown in the snapshot at 500 ps. The foamy transient structure subsequently decomposes into separate clusters which gradually develop into well-defined spherical liquid droplets. As evident from the snapshot taken at the end of the simulation, at 1 ns, the processes of the development of the largest droplets and relaxation of the liquid splashes induced by laser ablation last longer than the 1 ns duration of the simulation.

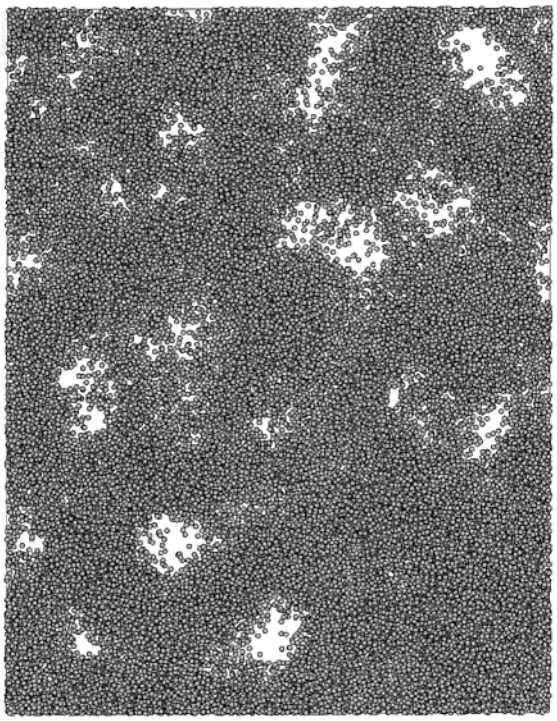

Figure 8. A closer look at the foamy transient structure of interconnected liquid clusters and individual molecules formed in the process of explosive homogeneous boiling of overheated material. A slab of dimensions 40 × 10 × 50 nm is cut from the ablation plume obtained in the simulation illustrated in Figure 7 at a time of 200 ps. The data are from ref 78 (Copyright 2003 Springer).

The picture of the homogeneous expansion of the overheated material and spontaneous decomposition into individual molecules and liquid droplets described above is consistent with the explosive vaporization mechanism predicted from classical thermodynamics.[136−141] As discussed in detail by Kelly and Miotello,[138−140] short pulse laser irradiation can overheat a part of the absorbing region beyond the limit of thermodynamic stability of the target material, leading to the onset of intense temperature, pressure, and density fluctuations. The fluctuations in the thermodynamically unstable material do not disappear but grow, leading to a rapid phase transition of the overheated material into a mixture of gas phase molecules and liquid droplets. The relative amount of the gas phase molecules is related to the degree of overheating[136] and provides a driving force for the expansion of the ablation plume. In the simulations performed with a 150 ps laser pulse in the thermal confinement regime, the fraction of individual molecules in the ejected plume indeed decreases from 25% at the maximum fluence studied, 86 J/m^2, to 9% at the threshold for ablation, 37 J/m^2. In the simulations performed close to the ablation threshold, the expansion of a relatively small gas phase fraction of the plume barely provides the momentum for ejection of only several large clusters that attain relatively low ejection velocities of less than 200 m/s.[69,78] The ablation threshold in the regime of thermal confinement is defined, therefore, by the overheating of the absorbing volume up to the point at which the explosive nucleation of the gas phase is sufficient for the ejection of liquid droplets. Simulation results

demonstrate that it is the onset of the cluster ejection that is responsible for the jump in the total amount of the ejected material at the ablation threshold, Figure 6, and that the cluster ejection is a characteristic feature of the ablation regime. The dynamics of the cluster formation in laser ablation and the parameters of the ejected clusters are discussed in Section IV.

Experimental observations of the existence of a well-defined threshold fluence for the onset of the cluster/droplet ejection, as well as a steep increase of the ablation rate at the threshold can be, therefore, interpreted as evidence of the transition from normal vaporization to phase explosion.[28,142−144] For organic targets, cluster ejection have been studied in trapping plate experiments performed by Handschuh et al.[28] for the UV-MALDI conditions, laser-induced thermal desorption, and infrared (IR) polymer ablation. The fluence dependence of the ejection of submicron sized particles observed for the UV-MALDI conditions, namely, no particle ejection below the ablation threshold, appearance of particles right above the threshold and decreased particle size at higher laser fluences, is consistent with the simulation results discussed above. For polymer ablation, the generation of charged clusters of different sizes, from submicron to 10 μm has been observed by Heitz and Dickinson.[29] The observed particles have been separated into several distinct classes based on the particle morphologies, composition, and electrostatic charge. Indirect evidence of the ejection of molecular clusters in MALDI has been obtained in post-ionization time-of-flight mass spectrometry experiments by Hankin and John.[145] Recent observations by Fournier et al.[146] of a nonlinear dependence of the time-of-flight from the delay time in the delayed extraction experiments has been explained by a delayed ion formation from higher mass precursors. A possible role of cluster ejection in the ionization processes in MALDI has been discussed in a number of works.[146−149]

Another important consequence of the phase explosion, revealed in the simulations, is the fast cooling of the ejected plume. As a measure of the average temperature in the plume we use the radial (parallel to the surface) velocity components of the ejected molecules, which do not contain contribution from the flow velocity of the plume. We find that the distributions of radial velocities fit well to a Maxwell−Boltzmann distribution,[63,65,69] verifying that the spread in the radial velocities is associated with the thermal motion in the plume. The average radial kinetic energy, calculated from the radial velocities of the molecules that were originally located in the top 18 nm layer of the irradiated sample is shown in Figure 9 for simulations performed with a laser pulse duration of 150 ps and fluences of 39 J/m^2 (just above the ablation threshold fluence) and 61 J/m^2 (1.75 times the ablation threshold fluence). Examining first the high fluence simulation, we observe a nearly linear increase of the radial kinetic energy during the laser pulse, followed by a fast drop of the energy during ~100 ps after the end of the laser pulse and a more gradual cooling occurring on the time scale of the simulation. In this simulation, the whole region

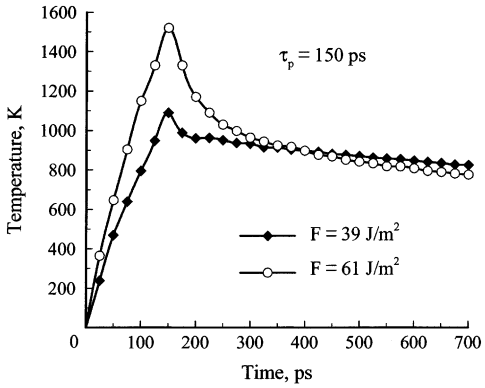

Figure 9. Averaged radial kinetic energy (in temperature units) of the molecules that belong to the top 18 nm layer of the original sample for simulations performed with laser pulse duration of 150 ps and fluences of 39 J/m^2 (just above the ablation threshold fluence) and 61 J/m^2 (1.75 times the ablation threshold fluence). The data are from ref 69 (Copyright 2000 American Institute of Physics).

over which the energy is averaged ablates and the fast cooling can be attributed to the explosive disintegration and ejection of the overheated material. The phase explosion, identified above as the dominant mechanism of laser ablation in the regime of thermal confinement, leads to the fast and efficient transfer of the kinetic energy of thermal molecular motion into the potential energy of material disintegration and the flow energy of the ejected plume. When less energy is deposited, a smaller degree of overheating is reached by the end of the laser pulse, and a less violent explosion occurs. As a consequence, the temperature maximum is lower in the simulation with 39 J/m^2 and the temperature drop is less dramatic. The gradual cooling that follows the temperature drop caused by the phase explosion is slower in the simulation performed with the lower fluence and, by the time of 500 ps, the average temperature of the region becomes even higher than the one for irradiation with the higher fluence. This can be explained by the fact that in the simulation with 39 J/m^2 the total amount of ejected material corresponds to only 11.4 nm layer of the original sample (~37% of the particles over which the averaging has been made still remain in the target) and a single large droplet constitutes the largest part of the total yield.[69] Evaporation of the large droplet and thermal conduction into the bulk of the sample provide a slower cooling as compared to the cooling of the rapidly expanding plume of small clusters and individual molecules formed in the simulation with 61 J/m^2. Temperature profiles similar to the ones shown in Figure 9 have been predicted for the phase explosion model of ion bombardment desorption/ablation[141] and have been observed in recent simulations of the explosive boiling of water films adjacent to hot metal surfaces,[99,100] as well as in earlier two-dimensional MD simulations of laser ablation[61,64] and ion bombardment.[150] In all cases, the fast cooling is attributed to the phase explosion of the overheated material. The fast cooling and the short time in the overheated state could be important factors responsible for survivability of large analyte molecules in MALDI.

C. Photomechanical Effects

In the discussion of the simulation results given in the previous subsections, the desorption and ablation processes are assumed to have purely thermal character (thermal desorption, melting, overheating, and explosive boiling) and are directly related to the energy density deposited by the laser pulse in the surface region of the irradiated target. The transition between desorption and ablation regimes as well as the amount of ejected material is completely defined by the laser fluence, initial temperature and absorption coefficient, eqs 1 and 2. The results of MD simulations performed with a shorter, 15 ps pulse, suggest, however, that in addition to the amount of energy supplied by the laser pulse and to the distribution of the energy within the sample, the rate of the energy deposition is an important factor affecting the ablation mechanisms and the parameters of the ejected plume.[68,69,71,78] In particular, we observe that in the regime of stress confinement, when the laser pulse duration becomes shorter than the time of the mechanical equilibration of the absorbing volume (see Section III.E.2), a high thermoelastic pressure builds up during the fast energy deposition and photomechanical effects induced by the pressure relaxation start to play an important role in material ejection.

The contribution of photomechanical effects to the material ejection in the regime of stress confinement is apparent from comparison of the yield vs fluence dependences shown in Figure 6a,b for 15 and 150 ps laser pulses. Although the same energy density for a given fluence is deposited in both cases (thermal confinement is realized for both pulse durations, see Section III.E.2), the threshold fluence and the corresponding value of the critical energy density E_v^* in eq 2 are 22% lower for irradiation with 15 ps pulses as compared to the values for 150 ps pulses. The ablation yield for 15 ps pulses is also consistently higher than the one for 150 ps pulses for all fluences above the threshold fluence. The difference in the threshold fluences for the ablation onset can be illustrated by snapshots shown in Figure 5a,d. Although the laser fluence is lower in the simulation shown in Figure 5d, a large layer of material is ejected in this case, whereas molecular ejection in Figure 5a is limited to the intensive evaporation from the surface. In other words, ablation is observed in the simulation illustrated by Figure 5d, whereas the simulation in Figure 5a is still in the desorption regime.

A visual analysis of the snapshots from the simulation in which the layer spallation takes place, Figure 10, clearly shows that the mechanism of material ejection in the case of 15 ps pulse is rather different from the homogeneous phase explosion responsible for the ablation onset in the case of longer, 150 ps pulse. In this simulation, we observe that shortly after the end of the laser pulse, a few voids are nucleated at a certain depth under the irradiated surface. The snapshots taken at 100 and 500 ps show coalescence and growth of the voids that eventually lead to the separation of a large surface layer from the bulk of the sample. The number of molecules in

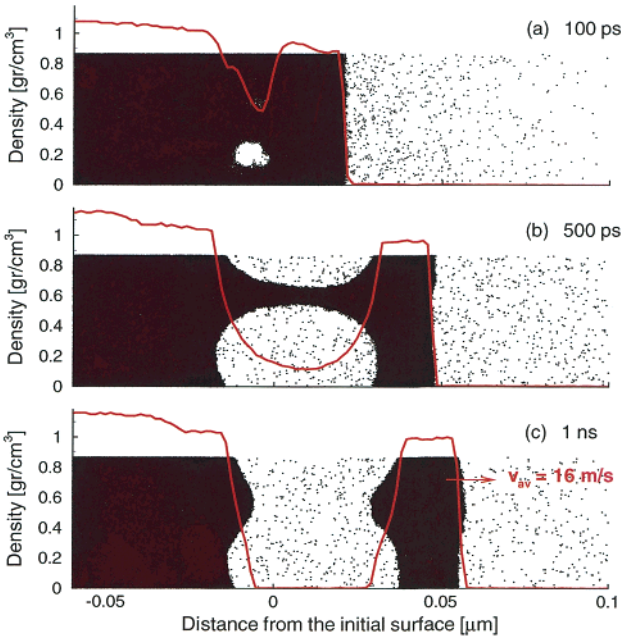

Figure 10. Density profiles near the surface of irradiated sample for simulation with 15 ps laser pulse and fluence of 31 J/m^2. Corresponding snapshots from the simulation are shown in the background of the density plots. The data are from ref 71 (Copyright 2001 Springer).

the ejected layer corresponds to a 16 nm layer of the original sample. By the time of 1 ns the layer is located at 50 nm above the original surface of the target and is moving from the target with a velocity of 16 m/s. The density of the gas-phase molecules between the layer and the remaining target is $\sim 1.5 \times 10^{19}$ molecules/cm^3 which is less than the density of an ideal gas under ambient conditions. The ejection and acceleration of the layer, therefore, are not affected by the expansion of the gas phase. The average temperature of the layer is 726 K, a value below the melting temperature of the model material, 750 K. An apparently viscous, liquidlike behavior observed in Figure 10 can be explained by the tensile stresses in the region of void formation that can locally reduce the melting temperature of the material.[151]

It is evident from the low temperature of the ejected layer and from the visual analysis of the snapshots given in Figure 10 that the physical processes leading to the material ejection have a mechanical rather than thermal character. The condition of stress confinement realized in the simulation results in the buildup of a high pressure within the absorbing region during the laser pulse. The pressure buildup can be seen in Figure 11, where the spatial distribution of the local hydrostatic pressure in the irradiated sample is shown for different times. A maximum compressive pressure as high as 470 MPa is reached in the absorption region shortly after the end of the laser pulse. Interaction of the laser-induced pressure with the free surface leads to the development of the tensile component of the pressure wave propagating from the absorption region deeper into the sample. In the case of elastic material response, the tensile component would increase with depth and would reach a maximum value equal to the compres-

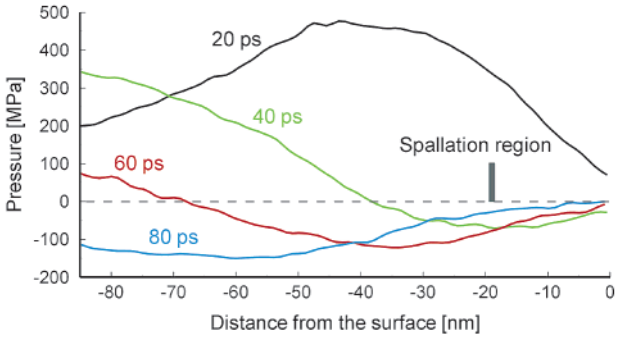

Figure 11. The spatial distribution of pressure in the MD computational cell at different times following irradiation by 15 ps laser pulse at laser fluence of 31 J/m^2. Snapshots from the simulation are shown in Figure 10. The nonreflecting boundary condition is applied at the depth of 90 nm as shown in Figure 3c. The data are from ref 71 (Copyright 2001 Springer).

sive component at approximately one penetration depth beneath the surface.[115,116,118] In the simulations performed at laser fluences above the threshold fluence, however, the tensile pressure exceeds the dynamic tensile strength of the material and causes mechanical fracture or spallation. The amplitude of the tensile component of the pressure wave is defined in this case by the dynamic tensile strength of the material and can be significantly lower than the one of the compressive component, Figure 11 (see also Section V). The microscopic mechanism of spallation observed in the simulations and consisting of nucleation, growth, and coalescence of voids is in a qualitative agreement with theoretical discussion of the spallation mechanism at high strain rates[82,152] as well as with predictions of molecular dynamics simulations of spallation in metals.[153,154]

The depth of the void nucleation and spallation, marked in Figure 11, is significantly closer to the surface than the depth at which the maximum tensile stresses are reached, ~50 nm or approximately one penetration depth beneath the surface. This observation can be explained by the strong temperature dependence of the ability of material to support tensile stresses. The tensile strength of the material heated by laser irradiation decreases significantly as the temperature approaches the melting temperature. The depth of the photomechanical damage, marked in Figure 11, is determined therefore by the balance between the tensile pressure that is increasing with depth and reaches −90 MPa in the spallation region and the decreasing thermal softening due to the laser heating. Although a significantly higher tensile pressure, up to −150 MPa, is reached deeper in the sample, it does not cause mechanical fracture of the colder and stronger material.

In simulations performed with 15 ps laser pulses in the stress confinement regime, the ejection of a surface layer of a sample is found to be the dominant process of laser ablation in a relatively wide range of fluences, from 29 J/m^2 up to 35 J/m^2. As the fluence increases within this interval, the void nucleation becomes less localized and is observed over a large surface region.[69,71] At higher laser fluences, above the threshold fluence for the ablation onset in the regime of thermal confinement, ~35 J/m^2, the material ejection is driven by the combination of the pressure gradient formed due to the stress confinement and the phase explosion due to the overheating, discussed in Section III.B. The effect of the stress confinement on the parameters of the ejected plume can be seen from density plots, Figure 12, where the number of peaks and their heights reflect the number of ejected clusters and their sizes, respectively.[69] Larger and more numerous clusters with higher ejection velocities are produced at the same laser fluence in the regime of stress confinement as compared to the regime of thermal confinement. The difference in the velocities of the ejected clusters is reflected in the difference in the spread in the positions of the peaks in Figure 12a,b. The density distribution of the gas-phase molecules, shown in the expanded view of the low-density region in Figure 12, is also different in these two simulations. The density of the cloud of individual molecules right above the surface observed in the simulation performed with a 15 ps pulse is less than half the density observed in the simulation performed with a 150 ps pulse. At the same time, a significantly higher density is observed in the simulation performed with a 15 ps pulse further from the surface, at distances of 1 μm and more. In the case of irradiation with 15 ps pulses, the cloud of individual molecules travels faster and disperses more during the same time after the end of the laser pulse. This observation can be attributed to the stronger pressure gradient that results from irradiation under the condition of stress confinement and provides higher initial acceleration to the ejected material. The differences in the parameters of the ejected plume, discussed above based on the density plots, can be confirmed by a visual analysis of the snapshots from the same simulations for which the density plots are given in Figure 12. In both simulations, the ejected material decomposes into liquid droplets and, by the time of 800 ps, when the snapshots are taken, most of the ejected plume is already located above the 40 × 40 × 150 nm region of the computational cell shown in the Figure 13. Nevertheless, we still see the final stage of the decomposition of the intermediate liquid structure into individual droplets and relaxation of the liquid near the surface. A much more forwarded ejection of liquid and a significantly lower density of the cloud of individual molecules are observed in Figure 13b as compared to Figure 13a.

The energetically efficient laser ablation predicted in the MD simulations can be related to experimental observations suggesting that a massive material removal or laser-induced cavitation and damage can be initiated at energy densities much lower than those required for boiling and vaporization.[14,33,115,116,155,156] Moreover, observations from scattering experiments for laser ablation of polymer targets by Hare et al.[157] suggest that photomechanical effects can lead to the ejection of a relatively intact layer of material that maintains its integrity at least on the time scale of tens of nanosecond. These observations can be related to the spallation of a layer of material observed in the simulations performed under conditions of stress confinement,[68,69,71] Figure 10. The role of photomechanical effects caused by the

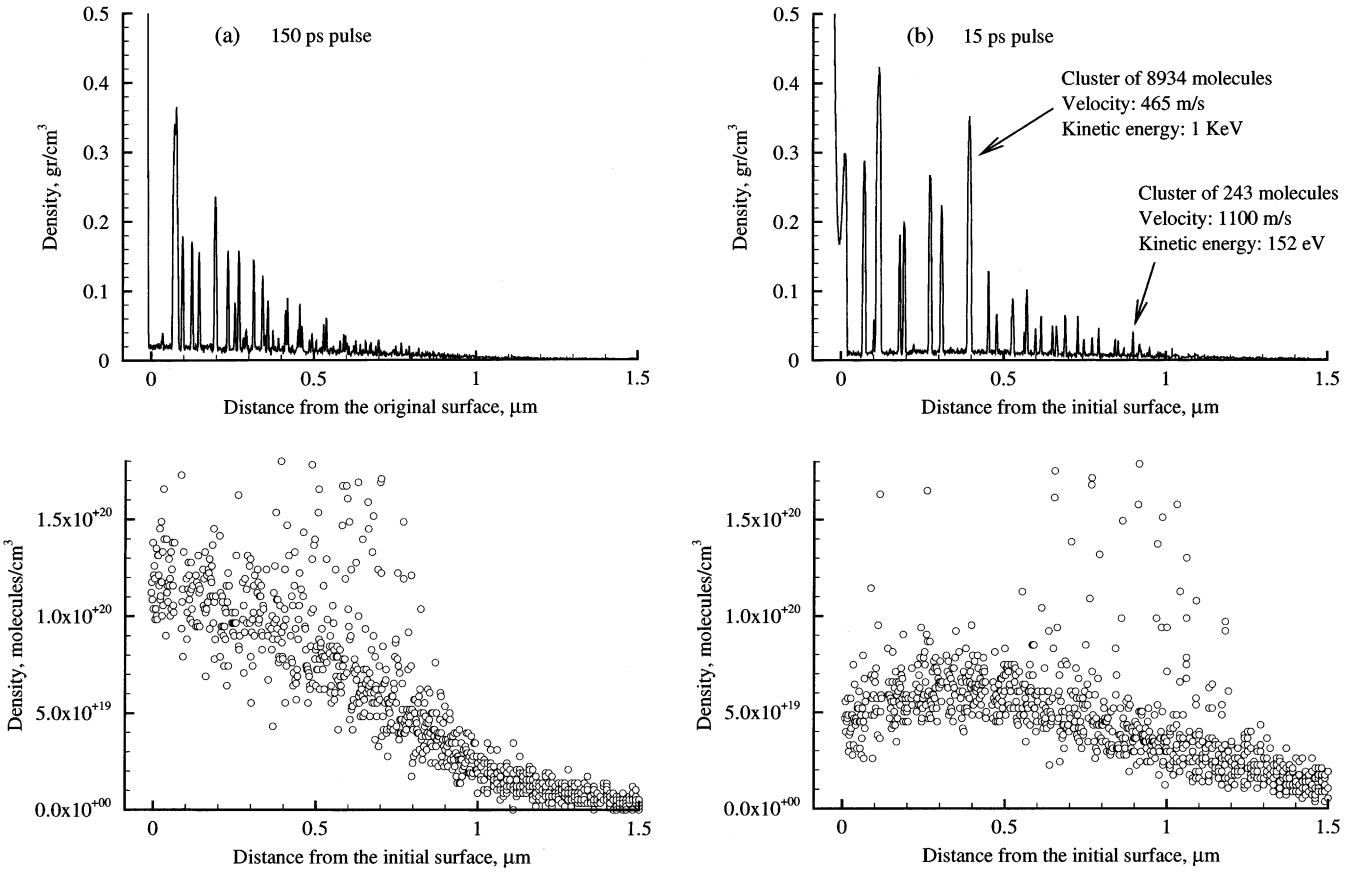

Figure 12. Density of the ejected plume as function of the distance from the initial surface for simulations with (a) 150 ps and (b) 15 ps laser pulses and fluence of 61 J/m^2 shown for the time of 850 ps after the end of the laser pulses. The lower frames show enlarged views of the low-density region of the upper frames, from 0 to 0.03 gr/cm^3, where the main contribution is coming from the gas-phase molecules. Each point in the lower frames results from the averaging over 1.5 nm span along the normal to the surface. The data are from ref 69 (Copyright 2000 American Institute of Physics).

relaxation of the laser-induced stresses and the mechanisms of photomechanical damage and spallation revealed in the simulations and discussed above are in agreement with a number of analytical calculations and theoretical discussions of the role of photomechanical effects in laser ablation and damage.[33,115,118,158−161]

D. Photochemical Effects

As described in Section II.C, the breathing sphere model has been adapted to include photofragmentation processes in 248 nm laser ablation of a chlorobenzene solid. Two sets of the molecular dynamics simulations with a different percentage of photofragmentation have been performed for a range of laser fluences. In the first system no photofragmentation occurs; therefore, all excited molecules undergo vibrational relaxation. The second system has 36% of excited molecules photofragmented, and the rest are vibrationally excited. This specific percentage has been observed experimentally for 248-nm irradiation of a molecular beam of chlorobenzene.[112]

The dependence of the amount of material removed per laser pulse versus fluence for these two systems is shown in Figure 14. Regardless of the presence of photochemistry, both systems exhibit two distinct mechanisms of ejection, desorption, and ablation, separated by the ablation threshold. It is noticeable that the molecular yield is higher and the ablation threshold is significantly lower for the system with photochemistry than for the system without photochemistry. A similar observation of a lower threshold fluence and higher ablation rates with photochemistry has been observed in experiments.[109,162]

As with the results presented in Figure 6, the yield vs fluence data in Figure 12 has been fit to the Arrhenius dependence, eq 1, in the desorption regime and to the critical energy density model, eq 2, in the ablation regime. The values of the activation energy in the desorption model, E_s, are 0.17 and 0.45 eV for calculations with and without photochemistry, respectively. The critical energy values in the ablation model are 0.22 and 0.53 eV for the two systems. The energy values with photochemistry are lower than those with only the thermal processes. One reason for the lowering of the critical energy values is that the addition of photochemistry creates an inhomegeneous system with lower cohesive energy in the absorbing region, thus reducing the ablation threshold.[73] In addition, as discussed in Section II.C, the photochemical reactions convert energy stored in chemical bonds into energy available for the ablation processes. The laser fluence thus is not a true measure of the energy available to induce ablation.

The magnitude of the additional energy available for the ablation process is shown in Figure 15 where the total enthalpy change per unit time is plotted vs time. In the system without reactions, the enthalpy

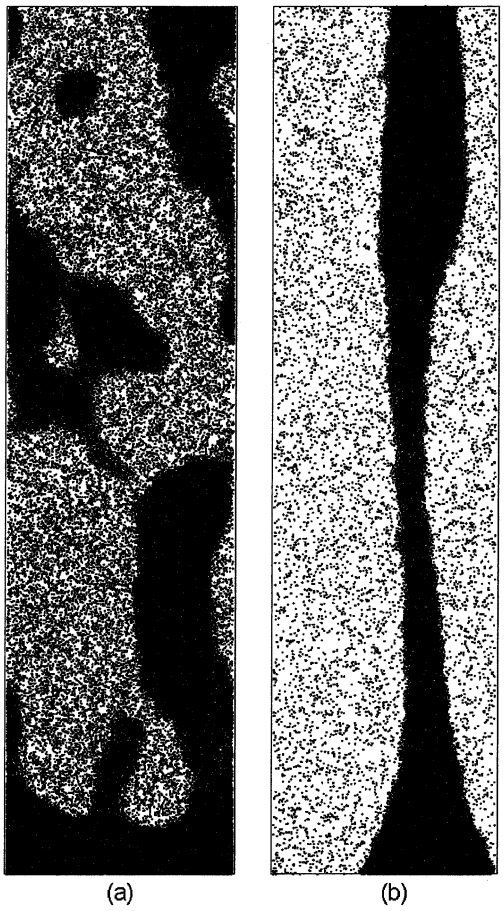

Figure 13. Snapshots from the simulations of laser ablation with 150 ps pulse (thermal confinement) and 15 ps pulse (stress confinement). The same fluence of 61 J/m^2 is used in both simulations and snapshots are taken at the same time of 800 ps after the beginning of the laser pulse. The data are from ref 78 (Copyright 2003 Springer).

deposited in the sample is directly defined by the laser fluence. In the case of the 248 nm irradiation, each photon absorbed increases the enthalpy by 482.7 kJ/mol. All of this energy is available for translational motions of the molecules as well as internal energy of the breathing mode. In the simulations with photochemistry, the enthalpy has an additional contribution from the chemical reactions. When the excited molecule undergoes fragmentation, most of the photon energy, 482.7 kJ/mol, goes to the bond rupture and the total enthalpy increases by only 79.5 kJ/mol. Thus, less energy is going into internal and translational molecular motions at the beginning of the laser pulse in the simulations with photochemistry as compared to the one with vibrational relaxation of excited molecules, Figure 15. During the first 10 ps, the amount of reactive photofragments is accumulating in the sample. When there is sufficient number of fragments formed inside the irradiated area and the temperature is sufficiently high, the fragments begin to react. These reactions are exothermic and release additional energy into the system, ranging from 30 kJ/mol up to 500 kJ/mol. The occurrence of the chemical reactions is responsible for the further increase of the enthalpy in the system. Although from Figure 15 it appears that the conversion of chemical energy into energy of motion might

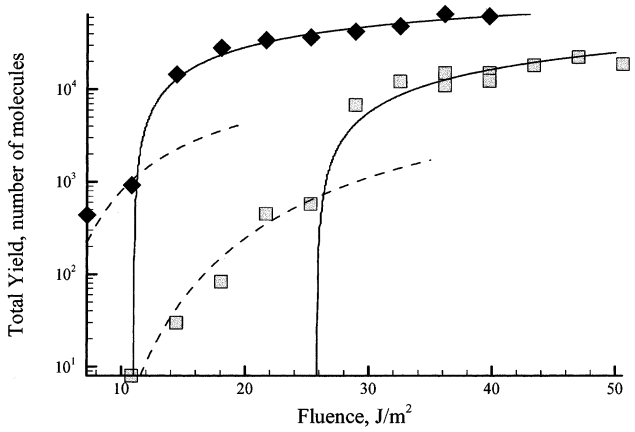

Figure 14. Total yield versus fluence dependence for simulations with vibrational relaxation of all excited molecules (gray squares) and with photofragmentation of 36% of the excited molecules (black diamonds) in a model chlorobenzene system. The solid lines represent prediction of the ablation model, eq 2, with $E_v^* = 0.53$ eV for the system with vibrational relaxation and $E_v^* = 0.22$ eV for the system with photofragmentation. The dashed lines represent the data fit to the thermal desorption model, eq 1, with $E_s^* = 0.45$ eV and $E_s^* = 0.17$ eV for systems with vibrational relaxation and photofragmentation, respectively.

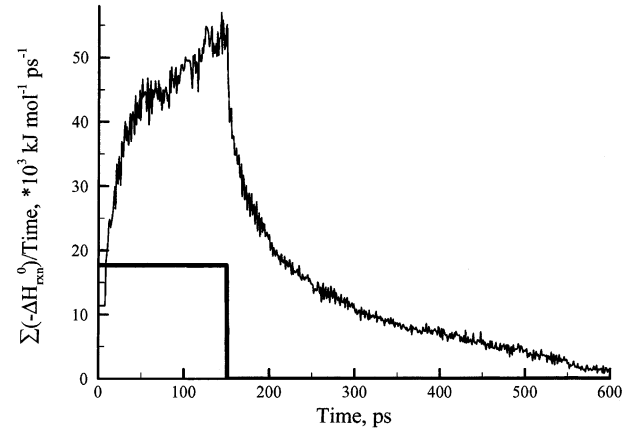

Figure 15. The rate of enthalpy change in the sample irradiated by a 150 ps laser pulse at laser fluence of 40 J/m^2. The thick straight line represents the system with vibrational relaxation of all excited molecules. The other line represents the system with photofragmentation of 36% of the excited molecules.

triple or quadruple the effective fluence, the probability of the reactions depends on the phase of the surroundings and the distance between the reactants, which is limited by the concentration of photofragmented molecules and mobility of fragments. Many energetic reactions are taking place only in the liquid and/or gas phase and most of the extra energy is deposited by reactions in the top layers of the sample and in the plume. After the laser pulse is over, no more photofragmentation reactions take place, but the existing radicals continue to react and the rate of energy deposition decreases gradually. There are other differences in the physical processes involved in laser ablation due to the presence of photochemistry that will be discussed in our further publications.

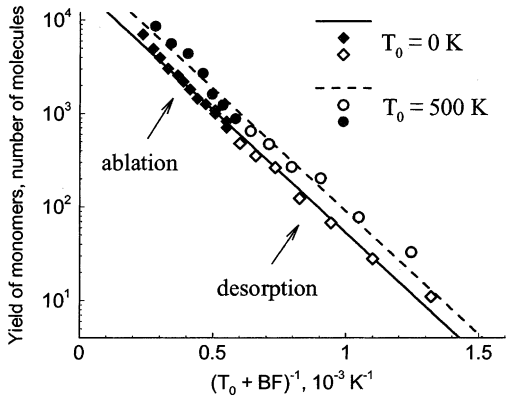

Figure 16. Arrhenius plots of the yield of monomers from simulations with two initial temperatures and laser pulse duration $\tau_p = 150$ ps. The diamonds and circles represent the data points for $T_0 = 0$ K and $T_0 = 500$ K, respectively. The open and closed symbols show the data points below and above the threshold for ablation. The solid and dashed lines represent fits of the data for $T_0 = 0$ K and $T_0 = 500$ K to the thermal desorption model, eq 1, with the same activation energy of 0.52 eV. The data are from ref 68 (Copyright 1999 Springer).

E. Dependence on the Irradiation Parameters

The ablation/desorption mechanisms revealed in MD simulations and discussed above have a strong dependence on the irradiation conditions and the initial state of the sample. Below we give a short summary of the dependence of the character of material ejection on laser fluence, pulse duration, and the initial temperature of the sample.

1. Laser Fluence

The most prominent feature of the yield vs fluence dependences observed in the simulations is the stepwise increase in the total amount of the ejected material at the threshold fluence.[61,62,64,67−69] The threshold behavior has been consistently observed in all simulations performed to date. In particular, qualitatively similar yield vs fluence dependencies shown in Figures 6 and 14 are obtained in simulations performed with 150 and 15 ps laser pulses, with different initial temperatures of the sample, and with and without photofragmentation of absorbing molecules. In all cases there are two distinct regimes of molecular ejection, desorption and ablation, that are separated by a well-defined threshold fluence.

Analysis of the composition of the ejected plume below and above the ablation threshold indicates that it is the onset of the ejection of large clusters that is responsible for the jump in the total yield at the threshold fluence. As we can see from the fluence dependence of the yields of monomers given in Figure 16, there is no step increase in the number of ejected monomers at the ablation threshold and one can hardly identify the threshold fluences from these plots. An Arrhenius-type dependence of the monomer yield on fluence given by eq 1 provides a good description of the monomer yield in the whole range of fluences and for two different initial temperatures of the sample with the same value of activation energy. Despite the seemingly good fit of the monomer yield, the thermal desorption model, leading to eq 1, does not give a correct description of the ejection mechanism at high fluences, where a collective ejection or ablation occurs. The differences between the fluence dependence of the total yield and the yield of individual molecules should be taken into account in analysis of the experimental mass spectrometry measurements, where the yield of individual neutral molecules is measured in post-ionization experiments. In particular, the yield of post-ionized matrix molecules measured in MALDI experiment by Dreisewerd et al. is reported to follow the Arrhenius equation in a wide range of fluences.[15] Simulation results, however, suggest that a good fit to the Arrhenius equation does not necessarily mean that the thermally activated desorption from the surface is responsible for the molecular ejection. Since the transition from desorption to ablation is not reflected in the number of ejected monomers, it can easily remain unnoticed in a post-ionization experiment. An interpretation of the physical mechanisms of material ejection should not be based solely on the mass spectrometry data,[15,21] but should be complemented by measurements of other characteristics, such as shapes of the acoustic waves propagating from the absorption region[31−39,115] or cluster detection in fast imaging[109,116,162,163] and trapping plate[28] experiments.

2. Pulse Duration

As discussed in Section III.C, both experimental data and computer simulations indicate that the threshold fluence for the ablation onset, the ablation mechanisms, and the parameters of the ejected plume have a strong dependence on the laser pulse duration. In this section, we outline the conditions that define the transitions between different ablation regimes.[69]

For long laser pulses, the redistribution of the absorbed laser energy by thermal conduction takes place during the laser pulse. As a result, the energy density deposited in the absorption region by the end of the laser pulse is inversely proportional to the square root of the pulse duration, τ_p. One can expect that in this regime of *thermal relaxation* the ablation threshold fluence would increase as the square root of the pulse duration, $F_{th}^{t.r.} \sim \sqrt{\tau_p}$. As the pulse duration becomes shorter than the time of the dissipation of the absorbed laser energy by the thermal conduction, τ_{th}, the deposited energy becomes confined within the absorbing volume. The condition for the *thermal confinement* of the deposited laser energy can be expressed as $\tau_p < \tau_{th} = \{L_p^2\}/\{AD_T\}$, where D_T is the thermal diffusivity of irradiated material, L_p is the laser penetration depth or the size of the absorbing structure, and A is a constant defined by the geometry of the absorbing region. The pulse duration in the regime of thermal confinement is usually shorter than the time needed for the formation and diffusion of a gas-phase bubble in the process of heterogeneous boiling.[140,164] As a result, the absorbing material can be overheated much beyond the boiling temperature, turning a normal surface evaporation at low laser fluences into an explosive vaporization, or phase explosion, at higher fluences. One can expect that in the regime of thermal confinement

the ablation threshold fluence is defined by the critical energy density sufficient for the overheating of the surface layer up to the limit of its thermodynamic stability[136−139] and is independent of the pulse duration, $F_{th}^{t.c.} \approx$ const.

As has been discussed in Section III.C, the contribution of photomechanical effects can lead to the material ejection at energy densities much lower than those required for boiling and vaporization. The condition for the onset of "cold" laser ablation, usually referred as inertial[62,158,160] or *stress confinement*,[33,68,69,71,74,115,119,155] can be expressed as $\tau_p \leq \tau_s \sim L_p/C_s$, where C_s is the speed of sound in the irradiated material and τ_s is the characteristic time of the mechanical equilibration of the absorbing volume.[165] In the regime of stress confinement, the laser pulse duration is shorter or comparable to the time that is needed for a mechanical relaxation (expansion) of the absorbing volume and the laser heating takes place at nearly constant volume conditions, causing buildup of a high thermoelastic pressure. Relaxation of the laser induced pressure can cause spallation or cavitation within the absorbing region, and can eventually lead to the ejection of large and relatively cold pieces of material. Contribution of the photomechanical effects under conditions of stress confinement can result in a significant decrease of the ablation threshold fluence as compared to the thermal confinement conditions, $F_{th}^{s.c.} < F_{th}^{t.c.}$.

In the simulations discussed above, the values of the laser pulse duration, 15 and 150 ps, are chosen to make sure that the simulations are performed in two distinct irradiation regimes, stress confinement and thermal confinement. The pulse duration of 150 ps is short relative to the characteristic thermal diffusion time across the absorption depth, $\tau_{th} \sim 10$ ns, but longer than the time of the mechanical equilibration of the absorbing volume, $\tau_s \sim 20$ ps. Thus, the simulations performed with 150 ps pulses are in the regime of thermal confinement but not thermoelastic stress confinement. For the 15 ps laser pulse, the condition for stress confinement, $\tau_p \leq \tau_s$, is satisfied.

A strong pulse width dependence of the mechanisms of laser ablation and damage has been also observed in heterogeneous materials, where the laser energy is deposited within spatially localized absorbers embedded into a transparent medium (e.g., melanin granules in pigmented tissues of the eye and skin).[166,167] Computer simulations of laser irradiation on an isolated submicron particle[168] and a particle embedded into a transparent medium[119,169] suggest that the onset of photomechanical effects under conditions of stress confinement is responsible for the decrease of the threshold fluence for laser ablation and damage observed for short laser pulses. Relaxation of the laser-induced pressure can lead to the mechanical disruption of the absorbers and emission of a strong pressure waves to the surrounding transparent medium.

3. Initial Temperature of the Sample

The initial temperature of the sample appears as a parameter in both eq 1 and eq 2, presenting a possibility to test the underlying physical picture of laser desorption and ablation by performing simulations at different temperatures. Figures 6b,c and 16 show yield vs fluence dependencies for total and monomer yields obtained in simulations performed with the same irradiation parameters for two initial temperatures, $T_0 = 0$ K and $T_0 = 500$ K.[68] Applying eqs 1 and 2 to describe the simulation data, we find that the same activation energies E_s^* and E_v^*, obtained from the fits to the data for zero temperature simulations, provide a good representation of the simulation data for $T_0 = 500$ K. This quantitative agreement between simulation results with different initial temperatures supports the description of the yield vs fluence dependence given by eqs 1 and 2 as well as the underlying physical mechanisms of molecular ejection.

Experimentally, a linear decrease of the detection threshold with increasing sample temperature has been observed for both neutral molecules and ions.[21] The detection threshold for neutral molecules in mass spectrometry experiments can be related to the lowest laser fluences at which a noticeable number of molecules desorb from irradiated surface in the simulations ($\sim$15 J/m^2 at $T_0 = 0$ K and $\sim$5 J/m^2 for $T_0 = 500$ K). The detection threshold for ions is more difficult to relate to the simulation data. We can speculate, however, that, since both threshold fluences and yield−fluence dependencies for matrix ions and analyte molecules in MALDI are nearly identical,[15] it is plausible to relate the detection threshold for matrix ions and analyte molecules to the ablation threshold, F_{th}, in the simulations ($\sim$35 J/m^2 at $T_0 =$ 0 K and $\sim$25 J/m^2 for $T_0 = 500$ K). Indeed, the large analyte molecules in MALDI are unlikely to be ejected through the thermal desorption from the surface and their ejection should involve entrainment into the ablation plume of ejected matrix molecules. The linear dependence of the detection threshold on sample temperature observed experimentally for neutral molecules[21] does agree with eq 1 for thermal desorption. On the other hand, eq 2 for ablation also predicts a linear dependence of the ablation threshold on temperature, $F_{th} = L_p(E_v^* - CT_0)$, which could be related to the observed linear dependence of the detection threshold for matrix ions.

IV. Dynamics of the Plume Formation and Parameters of the Ablation Plume

The dynamics of the early stages of the ablation plume formation and the mechanisms of cluster ejection were recently investigated in detail in a series of large-scale MD simulations for both thermal confinement[78] and stress confinement[74] conditions. Spatially and time-resolved analysis of the appearance and growth of density fluctuations in a region of molecular solid overheated by pulsed laser irradiation[74,78] has provided insights into the microscopic mechanisms of material ejection. The dynamics of cluster formation is found to be different in different parts of the ablation plume and is related to the character of explosive disintegration of the material that originates from different depths under the surface and reaches different maximum tempera-

tures by the end of the laser pulse. In simulations performed at laser fluences well above the ablation threshold fluences, the material ejected from the top layers of the irradiated sample is highly overheated and quickly, within first 100 ps, decomposes into gas phase molecules and a relatively small fraction of very small clusters. Overheating becomes weaker with increasing depth under the surface and larger clusters are formed in the middle of the ejected plume as a result of the explosive material disintegration. As discussed in Section III and illustrated in Figures 7 and 8, the explosive material disintegration proceeds through the spontaneous appearance of density fluctuations leading to the formation of a transient foamy structure of interconnected liquid regions. The transient foamy structure subsequently disintegrates into separate liquid droplets. Material disintegration in the rear part of the plume proceeds through similar steps. The fraction of the liquid phase in this part of the plume, however, is larger and the formation of a few large droplets proceeds through a coarsening of the initial transient foamy structure formed at earlier times of the plume expansion. Coarsening of the liquid regions and formation of large droplets is nearly complete by 1 ns, although relaxation of the shape of the largest droplets takes somewhat longer time. The density of the slowly moving droplets in the tail of the plume is sufficiently high and one can expect that collisions between the droplets can lead to their coalescence[134,135] and formation of even larger droplets.

The difference in the cluster formation processes occurring in different parts of the plume results in the effect of spatial segregation of clusters of different sizes in the plume. This effect is illustrated in Figure 17, where distributions of individual molecules, medium-size, large, and very large molecular clusters are shown. The medium size clusters are localized in the middle of the expanding plume, whereas the larger clusters formed later during the plume development tend to be slower and are closer to the original surface.

Despite being ejected from deeper under the surface, where the energy density deposited by the laser pulse and the degree of the overheating are smaller, the larger clusters in the plume are found to have substantially higher internal temperatures as compared to the smaller clusters. This can be seen from Figure 18, where the internal temperature of clusters of different sizes is shown. The internal temperature of a cluster is defined from the kinetic energy of the translational molecular motion in the cluster center of mass frame of reference. Despite the large scattering of the data points for individual clusters, the overall tendency is clear—larger clusters in the plume have, on the average, substantially higher internal temperatures as compared to smaller clusters. The lower temperature of the smaller clusters can be attributed to a more vigorous phase explosion (a larger fraction of the gas-phase molecules is released due to a higher degree of overheating) and a fast expansion of the upper part of the plume that provides a more efficient cooling as compared to a slower cooling of the larger clusters due to the evaporation.

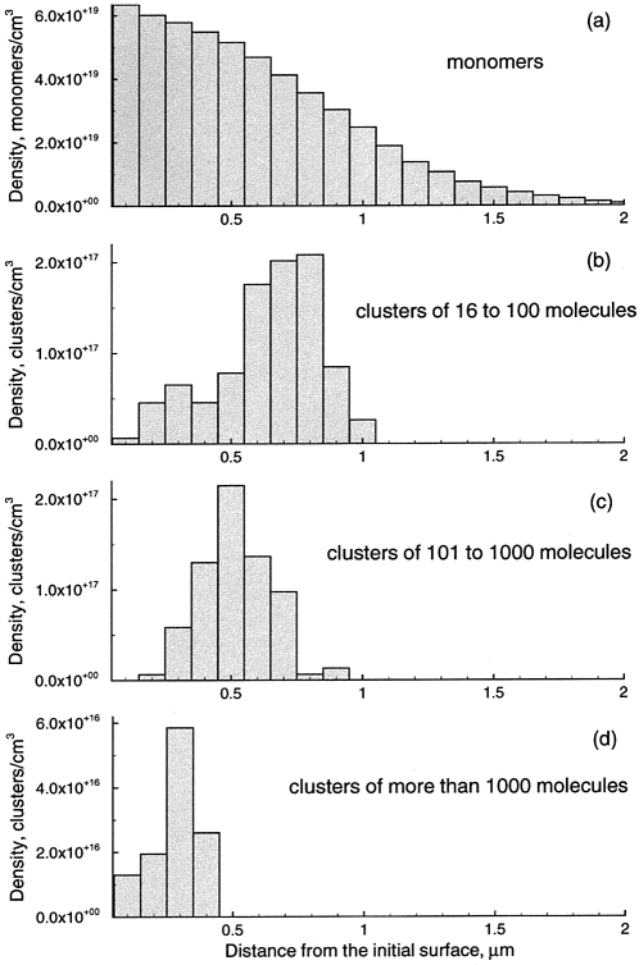

Figure 17. Number density of monomers and clusters of different sizes in the ablation plume as a function of the distance from the initial surface. The data are shown for 1 ns after irradiation with 150 ps laser pulse at laser fluence of 61 J/m^2. The distributions in (b), (c), and (d) are plotted for groups of clusters to obtain statistically adequate representations of the spatial distribution of large and medium clusters in the ablation plume. The data are from ref 78 (Copyright 2003 Springer).

The velocities of the ejected molecules and clusters can be described by the distribution of their radial (parallel to the surface) velocity components, as well as the flow velocities in the direction normal to the surface for different parts of the plume and for different plume components. The plot of the flow velocity as a function of the distance from the initial surface, Figure 19a, shows that identical linear dependencies on the distance from the surface, characteristic of the free expansion model, apply to all components of the plume. The clusters of different sizes are entrained into the expanding plume and are moving along with the individual molecules with nearly the same velocities. This effect of entrainment of molecular clusters can be related to the entrainment of large biomolecules into the plume of smaller matrix molecules in MALDI that has been observed experimentally[17,26,42,170−172] and in MD simulations.[65,70,75,76]

The spread in the radial velocities at a given distance from the surface can be described by a local translational temperature. The radial velocity components of molecules and clusters in the plume do

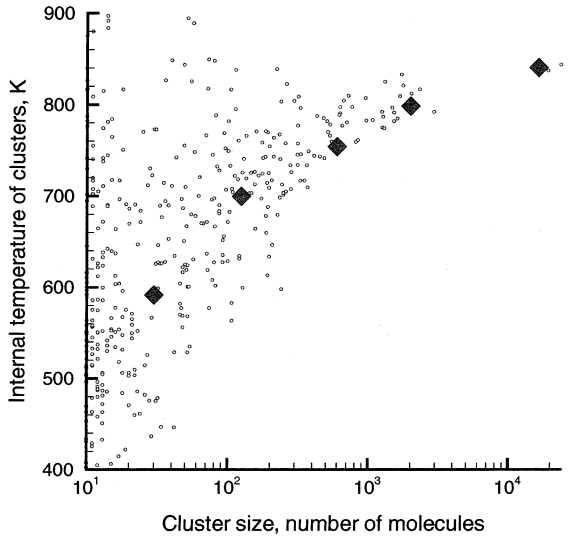

Figure 18. Internal temperature of clusters of different sizes (small circles).[78] The internal temperature of a cluster is defined from the kinetic energy of the translational molecular motion calculated in the cluster center of mass frame of reference. Five large diamonds show the average temperatures of clusters that belong to the following ranges of sizes: from 10 to 50, from 50 to 200, from 200 to 1000, from 1000 to 3000, and from 3000 to 30000 molecules. The data are shown for 1 ns after irradiation with 150 ps laser pulse at fluence of 61 J/m^2.

not contain a contribution from the forwarded flow of the plume in the direction normal to the surface and thus can be associated with the thermal motion in the plume. The radial velocity distributions of ejected molecules are found to fit well to a Maxwell−Boltzmann distribution verifying that the spread of the radial velocities is associated with thermal motion.[63,65,69] The plot of the translational temperature of monomers and clusters of different sizes, Figure 19b, suggests that the same local translational temperature can be used to describe the spread of the radial velocities of the ejected molecules, small and medium-size clusters in the dense part of the plume. The effect of the local thermal equilibration of different plume components can be related to the earlier results of MD simulations of MALDI, when the radial velocity distributions for both matrix molecules and analyte molecules of different masses were found to fit well to a Maxwell−Boltzmann distribution with the same temperature.[65] The radial velocities of larger clusters are found to be significantly higher as compared to the thermal velocities (not shown in Figure 19b). In particular, an average translational temperature calculated from the radial velocity component of clusters larger than 1000 molecules (there are 18 such clusters in the simulation for which data is plotted in Figure 19) is found to be as high as 3080 K. Apparently, the collisions with the surrounding smaller species in the plume are not sufficient for thermal equilibration of the radial velocities of the largest clusters. Rather, these velocities reflect the dynamics of the active hydrodynamic motion of the liquid material during the ablation plume formation.

A significant variation of the translational temperature with distance from the irradiated surface, observed in Figure 19b, indicates that the fast cooling of the ejected material proceeds nonuniformly within

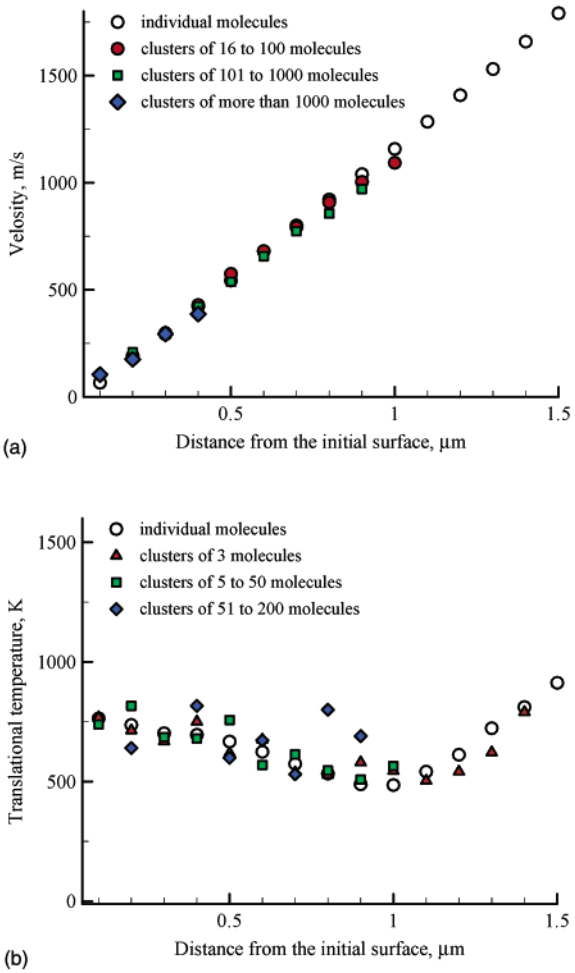

Figure 19. Flow velocity in the direction normal to the surface and translational temperature of different components of the ablation plume as a function of the distance from the initial surface.[78] (Copyright 2003 Springer) The translational temperature is calculated from the radial (parallel to the surface) velocity components of the ejected molecules or clusters. The data are shown for 1 ns after irradiation with 150 ps laser pulse at fluence of 61 J/m^2.

the plume. Explosive cooling, when the thermal energy is transformed to the potential energy of disintegration of the overheated material and to the kinetic energy of the plume expansion, proceeds more efficiently in the top part of the plume and leads to the decrease of the temperature in the flow direction. The same effect is responsible for the size dependence of the internal temperature of the ejected clusters shown in Figure 18 and discussed above. At a certain distance from the surface, the translational temperature of monomers and small clusters reaches its minimum and starts to increase. This temperature increase, that has been also observed in Monte Carlo simulations of multilayer particle ejection,[173] can be attributed to the lack of equilibration in the front part of the expanding plume, where densities of ejected species are too small. These fast particles can be considered to be promptly ejected beyond the outer boundary of the Knudsen layer.[47,174] Note, that although the average number of collisions per particle at the initial stage of the plume expansion is high enough to permit the formation of Knudsen layer, the relaxation of the laser-induced pressure gradient the target material, the explosive character of the abla-

tion plume formation, and monomer−cluster interactions have a profound influence on the final velocity distributions of molecules and clusters in the ablation regime which essentially differ from that predicted by gas expansion models. In particular, a drastic difference in the parameters of the ejected plume formed in the regimes of thermal and stress confinement at the same laser fluence[69] (and, therefore, the same maximum surface temperature) and a very high, up to 3 km/s, maximum flow velocity of monomers ejected in the stress confinement regime cannot be explained based on the gas-dynamic analysis and Knudsen layer concept.

The results shown in Figures 17−19 are obtained in a simulation performed with 150 ps laser pulse (thermal confinement regime) and laser fluence 1.75 times the ablation threshold fluence.[78] Qualitatively similar dependences are also observed in simulations performed with shorter, 15 ps laser pulses (stress confinement regime).[74] Quantitatively, for the same laser fluence and the same time after the laser pulse, the maximum axial velocities are ∼200 m/s higher and the translational temperatures are ∼100 K lower in the whole range of distances from the initial surface in the simulations performed in the regime of stress confinement as compared to the ones in the regime of thermal confinement.

V. Laser-Induced Pressure Waves

The differences in the mechanisms of material ejection in the regimes of thermal and stress confinement, discussed in Section III, are reflected in the parameters of the acoustic wave propagating from the absorption region deeper into the sample. Experimental piezoelectric measurements of laser induced acoustic signal indicate that the shape and the amplitude of the signal have strong dependence on the irradiation conditions.[31−39,115,116] The direct links between the results of photoacoustic measurements and complex processes in the absorption region, however, still have to be established. MD simulations provide an opportunity to perform a detailed analysis of the relations between the character of the molecular ejection in the regimes of thermal and stress confinement and the parameters of the pressure waves.

Temporal pressure profiles measured in MD simulations[69] are shown in Figure 20 for pulse durations of 15 and 150 ps and a wide range of fluences. The temporal pressure profiles are recorded at the depth of 100 nm under the initial surface in simulations where the total depth of the computational cell is 180 nm and the dynamic nonreflecting boundary condition is applied at the bottom of the computational cell. Similar to Figures 3 and 11, a positive pressure corresponds to compressive and a negative pressure to tensile stresses. Several observations can be made from the analysis of the pressure profiles shown in Figure 20.

First, the positive (compressive) amplitudes of the pressure waves are much higher in the regime of stress confinement as compared to the thermal confinement. This observation agrees with experimental observations that a significantly higher pressure builds up in the absorption region[157] and a much stronger acoustic signal is produced[36,37] when the conditions for stress confinement are satisfied. Several contributions to the compressive pressure can be identified in the simulations. One contribution is from the pressure wave that propagates from the irradiated surface. The wave is driven by thermoelastic stresses that build up in the absorption region during the laser pulse duration in the regime of stress confinement, as well as by the compressive recoil pressure imparted by the massive material ejection at fluences above the ablation threshold fluence. Another contribution to the compressive pressure is coming from the direct laser energy absorption at the depth of the pressure recording, 100 nm, that is only twice longer than the laser penetration depth. The small depth of the pressure recording results in a significant laser light absorption and corresponding buildup of thermoelastic stresses.[83] This contribution is reflected in the initial steep increase of the compressive pressure and asymmetric shapes of the compressive components of the pressure profiles. All the contributions to the compressive component of the recorded pressure profiles are much smaller in the regime of thermal confinement as

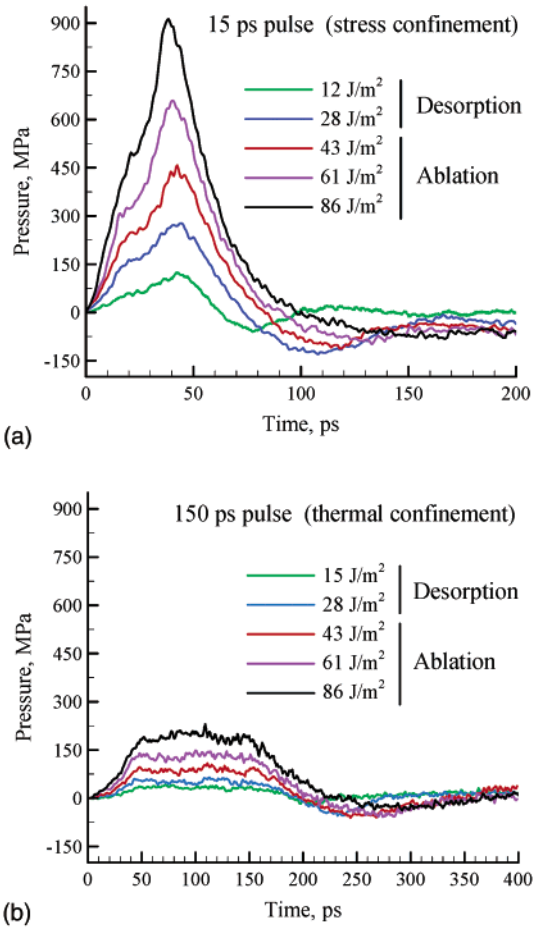

Figure 20. Temporal pressure profiles at 100 nm below the surface for simulations performed in regimes of (a) stress confinement and (b) thermal confinement. Computational cell with size of 180 nm in the direction normal to the surface is used in the simulations. The nonreflecting boundary condition[83] is applied at the bottom of the MD computational cell.

compared to the stress confinement. In the regime of thermal confinement, thermoelastic pressure has sufficient time to relax during the laser pulse duration (see Section III.E.2), whereas the ablation process is slower, spreading out the ablation recoil pressure over a longer time. The initial increase of the compressive pressure in Figure 20b can be attributed mainly to the direct laser energy deposition at the depth of recording. The pressure increases during the first 50 ps of the laser pulse and is balanced by the relaxation at later times.

Second, there is a clear difference in the pressure profiles recorded in the desorption and ablation regimes in the simulations performed with 15 ps laser pulse, Figure 20a. At low laser fluences, in the desorption regime, we observe a characteristic bipolar thermoelastic wave that results from the interaction of the laser-induced compressive thermoelastic pressure with free surface of the irradiated sample. A certain asymmetry between a stronger compressive component of the wave and a weaker tensile component in this case can be attributed to the contribution of the direct laser energy absorption at the depth of the recording, as discussed above. As the laser fluence increases above the threshold for the ablation onset, the ratio between the tensile and compressive components of the pressure wave gradually decreases and a strong unipolar compressive wave is generated at high laser fluences in the regime of stress confinement, Figure 20a.

Third, the fluence dependences of the compressive and tensile amplitudes of the pressure profile are drastically different. In simulations with both 15 and 150 ps pulses, the peak compressive pressure increases linearly with fluence as expected for thermoelastic mechanism of wave generation. The linear dependence extends beyond the ablation threshold, over the whole range of fluences, although the compressive recoil pressure imparted by the massive material ejection at high fluences leads to deviation of the amplitude of the compressive component of the pressure profiles from the linear dependence toward somewhat higher values at the highest laser fluences used in the simulations.[69] The amplitude of the tensile component of the pressure profile exhibits a more complex dependence on laser fluence. At low laser fluences, a linear increase of the peak tensile stresses with fluence is observed that corresponds to the expected increase of the amplitude of thermoelastic bipolar pressure wave. At higher laser fluences, however, the amplitude of the tensile component of the pressure profile saturates and even decreases with fluence. This behavior is apparent in Figure 20a, where the highest tensile pressure is recorded for laser fluence of 28 J/m^2, just below the threshold for the ablation onset. The existence of a maximum in the fluence dependence of the tensile pressure amplitude observed for 15 ps pulses is consistent with the discussion of the photomechanical processes responsible for the ablation onset in the regime of stress confinement given in Section III.C. The material ejection in this case is driven by the relaxation of the laser-induced pressure gradient and the observed maximum amplitude of the tensile stresses corresponds to the dynamic tensile strength of the material. A significant decrease of the amplitude of the tensile component of the pressure profile as laser fluence increases above the ablation threshold can be explained by contribution of the following two processes. First, the effect of thermal softening can significantly reduce the dynamic tensile strength of the material in the surface region of the sample at higher laser fluences, limiting the ability of the material to support the tensile stresses. Second, the tensile stresses produced by the thermoelastic mechanism can be obscured in the ablation regime by superposition with the compressive recoil pressure from the ejection of the ablation plume.

Experimentally, the pressure profiles similar to the ones shown in Figure 20a for 15 ps pulses have been observed for laser irradiation of soft biological tissue[37,38] and gelatine[115] below and above the ablation threshold fluence, respectively. The saturation or decrease of the amplitude of the tensile component of the pressure wave with increasing fluence has been observed for aqueous media irradiated in the stress confinement regime,[33,34] as well as in recent IR-MALDI experiments with glycerol as a MALDI matrix.[39] Both experimental measurements and the results of the present simulation study suggest that the shape and parameters of the acoustic wave propagating from the absorption region are sensitive to the changes in the mechanisms of material ejection and can be used for tuning of the irradiation parameters to the desired ejection conditions. Simulations allow us to directly relate the characteristics of the pressure waves to the molecular-level picture of laser desorption, ablation, and damage and can help in interpretation of experimental data from photoacoustic measurements.

VI. DSMC Simulation of the Ablation Plume Expansion

In this section, we present first results of DSMC simulations of the ablation plume expansion for the initial conditions obtained from the MD simulations. The results on the time evolution of the ablation plume in terms of the density profiles and distributions of internal energy of large clusters are presented and discussed.

In the absence of interaction with background gas and physical obstacles, the plume expansion should become self-similar in both axial and radial directions.[87,175] The driving forces and characteristic times of the formation of the self-similar flow, however, are different for the axial and radial directions and even the mechanisms of the self-similar flow formation in the radial direction are different for different plume components.

The collective character of the ablation process triggered by the relaxation of the laser-induced pressure[69] as well as intensive collisional processes within the initial dense plume are the main driving forces of the formation of the self-similar flow in the axial direction. The time of the formation of the self-similar multicomponent flow in the axial direction is on the order of several hundred picoseconds and

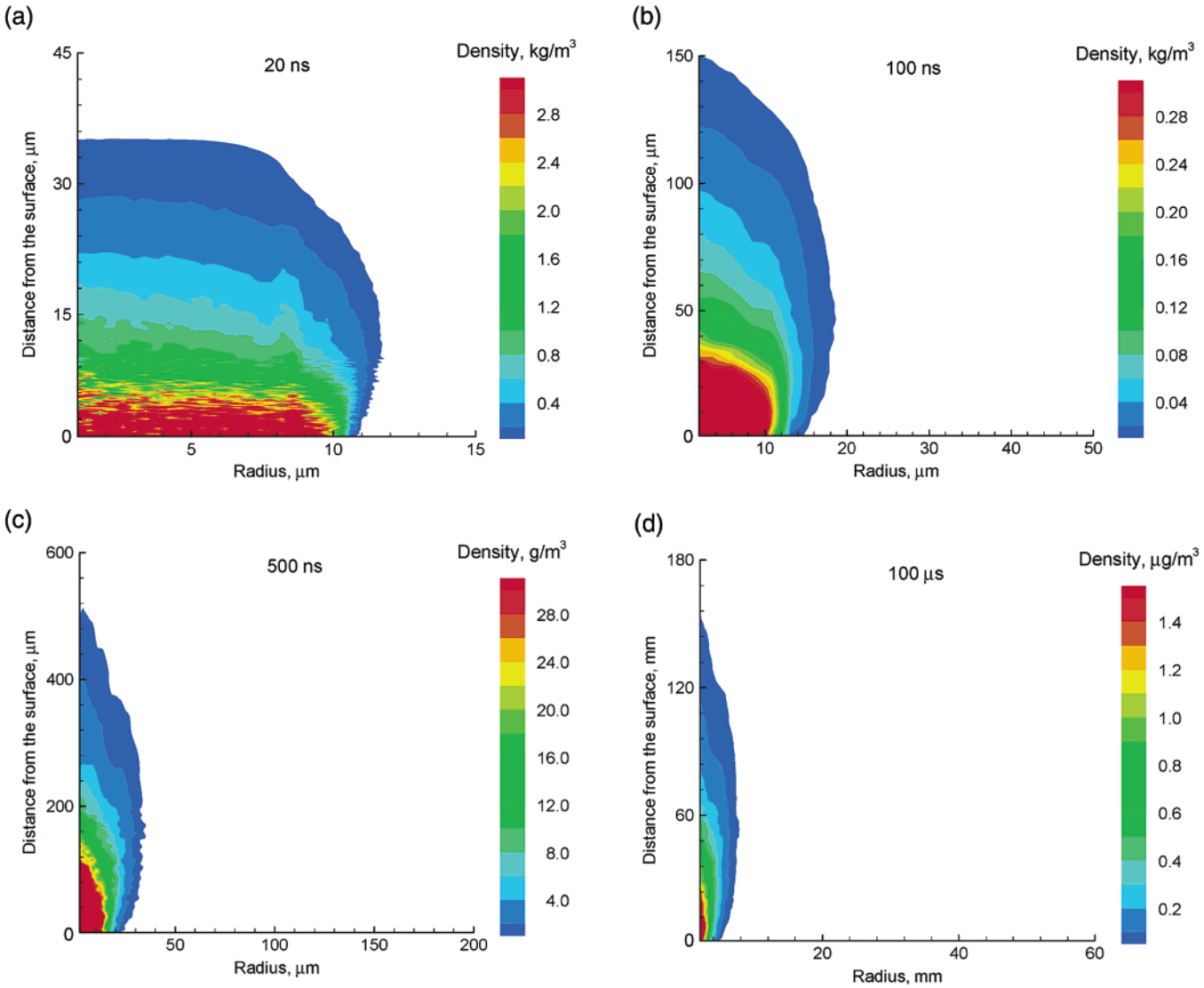

Figure 21. Time evolution of plume density at time 20 ns (a), 100 ns (b), 500 ns (c), and 100 μs (d). The aspect ratio is the same in all plots.

is established during the MD simulation, as shown in Figure 19a. At this time, different particles are characterized by the same flow velocities at the same height above the surface. At this stage of the plume evolution, the maximum height of the particles is small relative to the typical laser spot diameter,[69,78] and the expansion remains truly one-dimensional on the time scale of MD simulations.

The development of the radial flow in the multicomponent plume is described by the DSMC model. The process of formation of a self-similar flow of monomers in the radial direction is governed by the pressure gradient and the formation time is on the order of several tens of nanoseconds.[87] For the large clusters, the main driving force of the radial flow formation is collisions with monomers and light clusters. Because of the rapid plume expansion in the axial direction, the collision rate quickly subsides and the largest clusters acquire low radial velocities relative to their light counterparts,[87] which results in a sharpening of the overall density distribution of the ejected plume. This phenomenon has been observed in MALDI plume imaging experiments.[42]

Figure 21 visualizes the time evolution of the plume density as predicted in a DSMC simulation. As plume expands, the initial cylindrical plume changes its shape and becomes prolate elliptical. At time of 20 ns, the axial plume dimension is comparable with the radial dimension. Although the DSMC method accounts for both axial and radial expansions, the density shape is still fairly cylindrical at time of 20 ns. At times of 220 and 500 ns, the expansion in the radial direction becomes visible. The image extension along the axial coordinate is larger than that along the radial coordinate, which results in the effect of the sharpening of the density pattern mentioned above.

The expansion of the plume becomes self-similar at a time of 500 ns, when processes of interparticle reactions subside.[87] In self-similar expansion, the density profiles become geometrically similar when distances traveled by particles are large relative to the initial dimensions. Since the radial extension of the density profile at time 500 ns is on the order of the initial radius of the plume, the density patterns at time 100 μs and 500 ns are not geometrically similar. The final plume profile is strongly forward peaked with the aspect ratio of about 15.

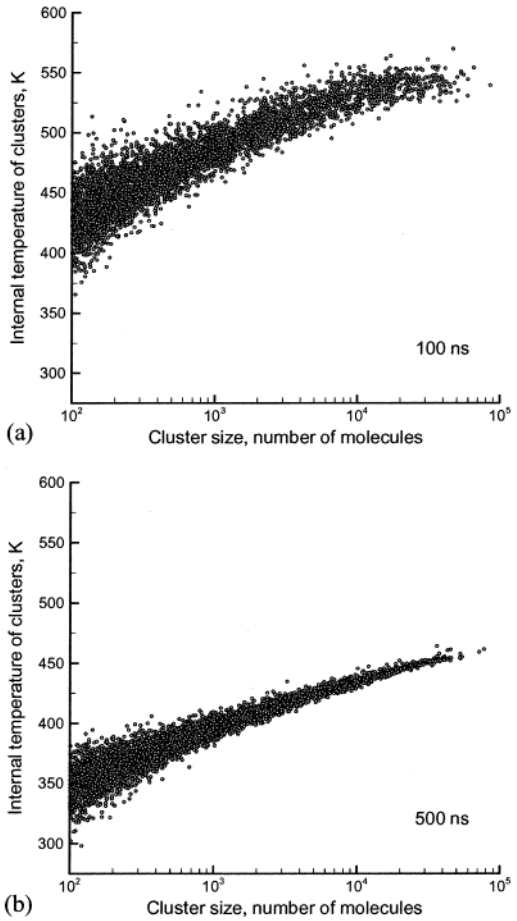

Figure 22. The cluster size dependence of the internal energy of large (more than 100 molecules) clusters at 100 ns (a) and 500 ns (b) after laser irradiation. The data are from ref 87 (Copyright 2002 American Institute of Physics).

Internal energy of large clusters is an important characteristic of the plume that defines the kinetics of evaporation/condensation processes and the results of cluster−cluster collision events during the long-term plume expansion. Figures 18 and 22 show the time evolution of the internal energy of large clusters. It is seen from the figures, that both mean temperature and statistical scatter of the temperatures decrease with time for each cluster size. The dependence of the mean internal temperature on the cluster size, however, does not become steeper with time. Rather, the temperature dependence tends to keep its shape during the cooling process. This phenomenon can be attributed to the fact that the rate of unimolecular cluster decomposition depends exponentially on both evaporation energy and internal temperature of the cluster and a steady slow cooling at times larger than 100 ns is only possible when the dependence of internal temperature on the cluster size will follow the cluster-size dependence of the evaporation energy.[87]

VII. Summary

The computational investigation of laser ablation of molecular systems is playing an increasingly important role in the development of a better theoretical understanding of the microscopic mechanisms responsible for the material ejection and their relationship to the parameters of the ablation process accessible for experimental investigation. The complexity of the laser ablation phenomenon and the multiscale character of the involved processes necessitate combination of different computational methods capable of addressing different aspects of laser ablation with appropriate temporal and spatial resolution. In particular, atomic-level MD simulations have been successfully used to study the channels and rates of the vibrational relaxation of molecules excited by laser irradiation and the redistribution of the deposited energy between the translational and internal degrees of freedom of molecules.

The information on the rates of the conversion of the internal energy of the excited molecules to the translational and internal motion of the other molecules has been used in parametrization of a coarse-grained "breathing sphere" model designed for large-scale MD simulations of laser ablation. The breathing sphere model has significantly expanded the time- and length-scales accessible for molecular-level simulations and provided an adequate description of the collective dynamic processes leading to laser ablation. The results obtained to date include prediction of a fluence threshold for ablation, identification of the processes responsible for material ejection in the regimes of thermal and stress confinement, a consistent analytical description of the velocity distributions for both matrix molecules and heavier analyte molecules in MALDI. The dynamics of the early stages of the ablation plume formation, the abundance of clusters and their distribution in the ejected plume, velocities of clusters and monomers, and other parameters of the ablation plume have been analyzed and related to the available experimental data. The shape and the amplitudes of the acoustic waves propagating from the absorption region have been studied and related to the ablation mechanisms and experimental piezoelectric measurements. The breathing sphere model has been recently extended to include a description of photochemical processes, such as photofragmentation of excited molecules, formation of radicals and subsequent abstraction and recombination reactions. First studies of the effect of the photochemical processes on ablation mechanisms have been performed.

A combined MD−DSMC computational model has been developed for simulation of the long-term plume expansion. First results of the combined MD-DSMC simulations demonstrate the ability of the method to follow the evolution of the parameters of the ablation plume on the scales characteristic for experimental investigations, up to hundreds of microseconds and millimeters. Gradual changes in the velocity and angular distributions of the ejected species and in the relative fractions of plume components, monomers and clusters of different sizes, can be investigated in the simulations.

While the computational studies reviewed in the present paper have provided valuable insights into the mechanisms of laser ablation of molecular systems, many questions still remain to be addressed. In particular, more accurate atomic level simulations are needed to investigate/explain the differences

between different molecular systems and to address an important issue of ionization. At the mesoscopic level, described by the breathing sphere model, further investigations of role of the photochemistry and thermochemistry in the ablation process, as well as the effect of the structure and composition of the initial sample are among the directions for future computational studies. A significant improvement of the combined MD-DSMC method is needed to obtain a reliable quantitative description of complex processes occurring during the multicomponent ablation plume expansion, such as cluster−cluster collisions, cluster evaporation/growth, chemical reactions, ionization, and ion extraction by an external field.

VIII. Acknowledgment

Financial support of this work was provided by the Air Force Office of Scientific Research through the Medical Free Electron Laser Program, the National Science Foundation, and the University of Virginia through the new faculty start-up funds.

IX. References

(1) Hillenkamp, F.; Karas, M. *Int. J. Mass Spectrom.* **2000**, *200*, 71.
(2) *Methods and Mechanisms for Producing Ions from Large Molecules*; Standing, K. G., Ens, W., Eds.; NATO ASI Series 269; Plenum Press: New York, 1991.
(3) Johnson, R. E. In *Large Ions: Their Vaporization, Detection and Structural Analysis*; Baer, T., Ng, C. Y., Powis, I., Eds.; John Wiley: New York, 1996; p 49.
(4) Niemz, M. H. *Laser-tissue Interactions: Fundamentals and Applications*; Springer-Verlag: Berlin Heidelberg, 1996.
(5) Bäuerle, D. *Laser Processing and Chemistry*; Springer-Verlag: Berlin Heidelberg, 2000.
(6) *Pulsed Laser Deposition of Thin Films*; Chrisey, D. B., Hubler, G. K., Eds.; Wiley-Interscience: New York, 1994.
(7) Hobley, J.; Fukumura, H.; Goto, M. *Appl. Phys. A* **1999**, *69*, S945.
(8) Zafiropulos, V.; Fotakis, C. In *Laser Cleaning in Conservation: an Introduction*; Cooper, M., Ed.; Butterworth Heinemann: Oxford, 1998; p 79.
(9) Lassithiotaki, M.; Athanassiou, A.; Anglos, D.; Georgiou, S.; Fotakis, C. *Appl. Phys. A* **1999**, *69*, 363.
(10) Lippert T.; David C.; Hauer M.; Wokaun A.; Robert J.; Nuyken O.; Phipps C. *J. Photochem. Photobiol. A* **2001**, *145*, 87.
(11) Dreisewerd, K.; Schürenberg, M.; Karas, M.; Hillenkamp, F. *Int. J. Mass Spectrom.* **1996**, *154*, 171.
(12) Menzel, C.; Dreisewerd, K.; Berkenkamp, S.; Hillenkamp, F. *J. Am. Soc. Mass Spectrom.* **2002**, *13*, 975.
(13) Demirev, P.; Westman, A.; Reimann, C. T.; Håkansson, P.; Barofsky, D.; Sundqvist, B. U. R.; Cheng, Y. D.; Seibt, W.; Siegbahn, K *Rapid Commun. Mass Spectrom.* **1992**, *6*, 187.
(14) Cramer, R.; Haglund, R. F., Jr.; Hillenkamp, F. *Int. J. Mass Spectrom.* **1997**, *169/170*, 51.
(15) Dreisewerd, K.; Schürenberg, M.; Karas, M.; Hillenkamp, F. *Int. J. Mass Spectrom.* **1995**, *141*, 127.
(16) Feldhaus, D.; Menzel, C.; Berkenkamp, S.; Hillenkamp, F.; Dreisewerd, K. *J. Mass Spectrom.* **2000**, *35*, 1320.
(17) Berkenkamp, S.; Menzel, C.; Hillenkamp, F.; Dreisewerd, K. *J. Am. Soc. Mass Spectrom.* **2002**, *13*, 209.
(18) Koubenakis, A.; Labrakis, J.; Georgiou, S. *Chem. Phys. Lett.* **2001**, *346*, 54.
(19) Westman, A.; Huth-Fehre, T.; Demirev, P.; Bielawski, J.; Medina, N.; Sundqvist, B. U. R. *Rapid Commun. Mass Spectrom.* **1994**, *8*, 388.
(20) Aksouh, F.; Chaurand, P.; Deprun, C.; Della-negra, S.; Hoyes, J.; LeBeyec, Y.; Pinho, R. R. *Rapid Commun. Mass Spectrom.* **1995**, *9*, 515.
(21) Schürenberg, M.; Dreisewerd, K.; Kamanabrou, S.; Hillenkamp, F. *Int. J. Mass Spectrom.* **1998**, *172*, 89.
(22) Yingling, Y. G.; Zhigilei, L. V.; Garrison, B. J.; Koubenakis, A.; Labrakis, J.; Georgiou, S. *Appl. Phys. Lett.* **2001**, *78*, 1631.
(23) Braun, R.; Hess, P. *J. Chem. Phys.* **1993**, *99*, 8330.
(24) Elam J. W.; Levy, D. H. *J. Phys. Chem. B* **1998**, *102*, 8113.
(25) Zhang W.; Chait, B. T. *Int. J. Mass Spectrom.* **1997**, *160*, 259.
(26) Glückmann M.; Karas, M. *J. Mass Spectrom.* **1999**, *34*, 467.
(27) Juhasz, P.; Vestal, M. L.; Martin, S. A. *J. Am. Soc. Mass Spectrom.* **1997**, *8*, 209.
(28) Handschuh, M.; Nettesheim, S.; Zenobi, R. *Appl. Surf. Sci.* **1999**, *137*, 125.
(29) Heitz, J.; Dickinson, J. T. *Appl. Phys. A* **1999**, *68*, 515.
(30) Heitz, J.; Arenholz, E.; Dickinson, J. T. *Appl. Phys. A* **1999**, *69*, S467.
(31) Dyer, P. E.; Srinivasan R. *Appl. Phys. Lett.* **1986**, *48*, 445.
(32) Srinivasan R.; Braren, B. *Chem. Rev.* **1989**, *89*, 1303.
(33) Oraevsky, A. A.; Jacques, S. L.; Tittel, F. K. *J. Appl. Phys.* **1995**, *78*, 1281.
(34) Karabutov, A.; Podymova, N.; Letokhov, V. *Proc. SPIE* **1996**, *2624*, 93.
(35) Kim, D.; Ye, M.; Grigoropoulos, C. P. *Appl. Phys. A* **1998**, *67*, 169.
(36) Kim, D.; Grigoropoulos, C. P. *Appl. Surf. Sci.* **1998**, *127−129*, 53.
(37) Venugopalan, V.; Nishioka, N. S.; Mikić, B. B. *Biophys. J.* **1995**, *69*, 1259.
(38) Venugopalan, V.; Nishioka, N. S.; Mikić, B. B. *Biophys. J.* **1996**, *70*, 2981.
(39) Dreisewerd, K.; Menzel, C.; Rolhfing, A.; Hillenkamp, F.; Kukreja, L. M. In *Proceedings of the 48th Conference on Mass Spectrometry and Allied Topics*; Chicago, Illinois, May 27−31, 2001.
(40) Kelly, R.; Miotello, A.; Braren, B.; Otis, C. E. *Appl. Phys. Lett.* **1992**, *60*, 2980.
(41) Fukumura, H.; Hatanaka, K.; Hobley, J. *J. Photochem. Photobiol. C* **2001**, *2*, 153.
(42) Puretzky, A. A.; Geohegan, D. B.; Hurst, G. B.; Buchanan, M. V.; Luk'yanchuk, B. S. *Phys. Rev. Lett.* **1999**, *83*, 444.
(43) Johnson, R. E.; LeBeyec, Y. *Int. J. Mass Spectrom.* **1998**, *177*, 111.
(44) Johnson, R. A.; Sundqvist, B. U. R. *Rapid Commun. Mass Spectrom.* **1991**, *5*, 574.
(45) Williams, P.; Nelson, R. W. In ref 2, p 265.
(46) Vertes, A. In ref 2, p 275.
(47) Kelly, R.; Miotello, A.; Braren, B.; Gupta, A.; Casey, K. *Nucl. Instrum. Methods B* **1992**, *65*, 187.
(48) Luk'yanchuk, B.; Bityurin, N.; Anisimov, S.; Arnold, N.; Bäuerle, D. *Appl. Phys. A* **1996**, *62*, 397.
(49) Bityurin, N.; Malyshev, A. *J. Appl. Phys.* **2002**, *92*, 605.
(50) Bityurin, N.; Luk'yanchuk, B.; Hong, M.; Chong, C. Review of continuum modeling of laser ablation of polymer in this issue of *Chemical Reviews*.
(51) Vertes, A.; Irinyi, G.; Gijbels, R. *Anal. Chem.* **1993**, *65*, 2389.
(52) Vertes, A.; Levine, R. D. *Chem. Phys. Lett.* **1990**, *171*, 284.
(53) Kelly, R.; Miotello, A.; Braren, B.; Otis, C. E. *Appl. Phys. Lett.* **1992**, *61*, 2784.
(54) Garrison, B. J.; Srinivasan, R. *Appl. Phys. Lett.* **1984**, *44*, 849.
(55) Garrison, B. J.; Srinivasan, R. *J. Appl. Phys.* **1985**, *57*, 2909.
(56) Bencsura A.; Vertes A. *Chem. Phys. Lett.* **1995**, *247*, 142.
(57) Bencsura A.; Navale V.; Sadeghi M.; Vertes A. *Rapid Commun. Mass Spectrom.* **1997**, *11*, 679.
(58) Wu, X.; Sadeghi, M.; Vertes, A. *J. Phys. Chem. B* **1998**, *102* 4770.
(59) Dutkiewicz, Ł.; Johnson, R. E.; Vertes, A.; Pędrys, R. *J. Phys. Chem. A* **1999**, *103* 2925.
(60) Sadeghi, M.; Wu, X.; Vertes, A. *J. Phys. Chem. B* **2001**, *105*, 2578.
(61) Zhigilei, L. V.; Kodali, P. B. S.; Garrison, B. J. *J. Phys. Chem. B* **1997**, *101*, 2028.
(62) Zhigilei, L. V.; Kodali, P. B. S.; Garrison, B. J. *Chem. Phys. Lett.* **1997**, *276*, 269.
(63) Zhigilei, L. V.; Garrison, B. J. *Appl. Phys. Lett.* **1997**, *71*, 551.
(64) Zhigilei, L. V.; Kodali, P. B. S.; Garrison, B. J. *J. Phys. Chem. B* **1998**, *102*, 2845.
(65) Zhigilei L. V.; Garrison, B. J. *Rapid Commun. Mass Spectrom.* **1998**, *12*, 1273.
(66) Kodali, P. B. S.; Zhigilei, L. V.; Garrison, B. J. *Nucl. Instrum. Methods B* **1999**, *153*, 167.
(67) Zhigilei, L. V.; Garrison, B. J. *Appl. Phys. Lett.* **1999**, *74*, 1341.
(68) Zhigilei, L. V.; Garrison, B. J. *Appl. Phys. A* **1999**, *69*, S75.
(69) Zhigilei L. V.; Garrison, B. J. *J. Appl. Phys.* **2000**, *88*, 1281.
(70) Itina, T. E.; Zhigilei, L. V.; Garrison, B. J. *Nucl. Instrum. Methods B* **2001**, *180*, 238.
(71) Zhidkov, A. G.; Zhigilei, L. V.; Sasaki, A.; Tajima, T. *Appl. Phys. A* **2001**, *73*, 741.
(72) Yingling, Y. G.; Zhigilei, L. V.; Garrison, B. J. *Nucl. Instrum. Methods B* **2001**, *180*, 171.
(73) Yingling, Y. G.; Zhigilei, L. V.; Garrison, B. J. *J. Photochem. Photobiol. A* **2001**, *145*, 173.
(74) Zhigilei, L. V. *Mater. Res. Soc. Symp. Proc.* **2001**, *677*, AA2.1.1.
(75) Itina, T. E.; Zhigilei, L. V.; Garrison, B. J. *J. Phys. Chem. B* **2002**, *106*, 303.
(76) Zhigilei L. V.; Yingling, Y. G.; Itina, T. E.; Schoolcraft, T. A.; Garrison, B. J. *Int. J. Mass Spectrom.*, in press.
(77) Zhigilei L. V.; Dongare, A. M. *Comput. Model. Eng. Sci.* **2002**, *3*, 539.
(78) Zhigilei, L. V. *Appl. Phys. A* **2003**, *76*, 339.
(79) Hill, J. R.; Chronister, E. L.; Chang, T.-C.; Kim, H.; Postlewaite, J. C.; Dlott, D. D. *J. Chem. Phys.* **1988**, *88*, 2361.

(80) Deàk, J. C.; Iwaki, L. K.; Rhea, S. T.; Dlott, D. D. *J. Raman Spectrosc.* **2000**, *31*, 263.
(81) Woutersen S.; Bakker, H. J. *Nature* **1999**, *402*, 507.
(82) Dekel, E.; Eliezer, S.; Henis, Z.; Moshe, E.; Ludmirsky, A.; Goldberg, I. B. *J. Appl. Phys.* **1998**, *84*, 4851.
(83) Zhigilei L. V.; Garrison, B. J. *Mater. Res. Soc. Symp. Proc.* **1999**, *538*, 491.
(84) Eliezer, S.; Gazit, Y.; Gilath, I. *J. Appl. Phys.* **1990**, *68*, 356.
(85) Smirnova, J. A.; Zhigilei, L. V.; Garrison, B. J. *Comput. Phys. Commun.* **1999**, *118*, 11.
(86) Zeifman, M. I.; Garrison, B. J.; Zhigilei, L. V. *Appl. Surf. Sci.* **2002**, *197*−*198*, 27.
(87) Zeifman, M. I.; Garrison, B. J.; Zhigilei, L. V. *J. Appl. Phys.* **2002**, *92*, 2181.
(88) Kim, H.; Dlott, D. D. *J. Chem. Phys.* **1991**, *94*, 8203.
(89) Kim, H.; Dlott, D. D.; Won, Y. *J. Chem. Phys.* **1995**, *102*, 5480.
(90) Kim, H.; Won, Y. *J. Phys. Chem.* **1996**, *100*, 9495.
(91) Nelson, R. W.; Rainbow, M. J.; Lohr, D. E.; and Williams, P. *Science* **1989**, *246*, 1585.
(92) Nelson, R. W.; Thomas, R. M.; Williams, P. *Rapid Commun. Mass Spectrom.* **1990**, *4*, 349.
(93) Schieltz, D. M.; Chou, C.-W.; Luo, C.-W.; Thomas, R. M.; Williams, P. *Rapid Commun. Mass Spectrom.* **1992**, *6*, 631.
(94) Williams, P. *Int. J. Mass Spectrom.* **1994**, *131*, 335.
(95) Talrose, V. L.; Person, M. D.; Whittal, R. M.; Walls, F. C.; Burlingame, A. L.; Baldwin, M. A. *Rapid Commun. Mass Spectrom.* **1999**, *13*, 2191.
(96) Tam, A. C.; Leung, W. P.; Zapka, W.; Ziemlich, W. *J. Appl. Phys.* **1992**, *71*, 3515.
(97) She, M.; Kim, D.; Grigoropoulos, C. P. *J. Appl. Phys.* **1999**, *86*, 6519.
(98) Lu, Y. F.; Song, W. D.; Zhang, Y.; Low, T. S. *Proc. SPIE* **1998**, *3550*, 7.
(99) Dou, Y.; Zhigilei, L. V.; Postawa, Z.; Winograd, N.; Garrison, B. J. *Nucl. Instrum. Methods B* **2001**, *180*, 105.
(100) Dou, Y.; Zhigilei, L. V.; Winograd, N.; Garrison, B. J. *J. Phys. Chem. A* **2001**, *105*, 2748.
(101) Williams, G. J.; Zhigilei, L. V.; Garrison, B. J. *Nucl. Instrum. Methods B* **2001**, *180*, 209.
(102) Zare R. N.; Levine, R. D. *Chem. Phys. Lett.* **1987**, *136*, 593.
(103) Banerjee, S.; Johnson, R. E.; Cui, S.-T.; Cummins, P. T. *Phys. Rev. B* **1994**, *43*, 12707.
(104) Zhigilei, L. V.; Srivastava, D.; Garrison, B. J. *Surf. Sci.* **1997**, *374*, 333.
(105) Wyatt, R. E.; Iung, C.; Leforestier, C. *Acc. Chem. Res.* **1995**, *28*, 423.
(106) Likhachev, V. A.; Mikhailin, A. I.; Zhigilei, L. V. *Philos. Mag. A* **1994**, *69*, 421.
(107) Allwood, D. A.; Dreyfus, R. W.; Perera, I. K.; Dyer, P. E. *Rapid Commun. Mass Spectrom.* **1996**, *10*, 1575.
(108) Georgiou, S.; Koubenakis, A.; Syrrou M.; Kontoleta, P. *Chem. Phys. Lett.* **1997**, *270*, 491.
(109) Georgiou, S.; Koubenakis, A.; Labrakis J.; Lassithiotaki, M. *J. Chem. Phys.* **1998**, *109*, 8591.
(110) Georgiou, S.; Koubenakis, A.; Labrakis J.; Lassithiotaki, M. *Appl. Surf. Sci.* **1998**, *127*, 122.
(111) Tsuboi, Y.; Hatanaka, K.; Fukumura, H.; Masuhara, H. *J. Phys. Chem.* **1994**, *98*, 11237.
(112) Tsuboi, Y.; Hatanaka, K.; Fukumura, H.; Masuhara, H. *J. Phys. Chem. A* **1998**, *102*, 1661.
(113) Ichimura, T.; Mori, Y.; Shinohara H.; Nishi, N. *Chem. Phys.* **1994**, *189*, 117.
(114) Davidson, R. S.; Goodin J. W.; Kemp, G. *Adv. Phys. Org. Chem.* **1984**, *20*, 191 and references therein.
(115) Paltauf, G.; Schmidt-Kloiber, H. *Appl. Phys. A* **1996**, *62*, 303.
(116) Paltauf, G.; Schmidt-Kloiber, H. *Proc. SPIE* **1992**, *1646*, 343.
(117) Etcheverry, J. I.; Mesaros, M. *Phys. Rev. B* **1999**, *60*, 9430.
(118) Dingus, R. S.; Scammon, R. J. *Proc. SPIE* **1991**, *1427*, 45.
(119) Zhigilei L. V.; Garrison, B. J. *Proc. SPIE* **1998**, *3254*, 135.
(120) Schäfer, C.; Urbassek, H. M.; Zhigilei, L. V.; Garrison, B. J. *Comput. Mater. Sci.* **2002**, *24*, 421.
(121) Rudd R. E.; Broughton, J. Q. *Phys. Rev. B* **1998**, *58*, R5893.
(122) Bird, G. A. *Molecular Gas Dynamics and the Direct Simulation of Gas Flows*; Clarendon Press: Oxford, 1994.
(123) Sibold D.; Urbassek, H. M. *J. Appl. Phys.* **1993**, *73*, 8544.
(124) Urbassek, H. M.; Sibold, D. *Phys. Rev. Lett.* **1993**, *70*, 1886.
(125) Economou, D. J.; Bartel, T. J.; Wise, R. S.; Lymberopoulos, D. P. *IEEE Trans. Plasma Sci.* **1995**, *23*, 581.
(126) Itina, T. E.; Marine, W.; Autric, M. *J. Appl. Phys.* **1997**, *82*, 3536.
(127) Itina, T. E. *J. Appl. Phys.* **2001**, *89*, 740.
(128) Oran, E. S.; Oh, C. K.; Cybyk, B. Z. *Annu. Rev. Fluid Mech.* **1998**, *30*, 403.
(129) Birdsall, C. K. *IEEE Trans. Plasma Sci.* **1991**, *19*, 65.
(130) Zhidkov, A. G. *Phys. Plasmas* **1998**, *5*, 541.
(131) Venkatesh, R.; Lucchese, R. R.; Marlow, W. H.; Schulte, J. *J. Chem. Phys.* **1995**, *102*, 7683.
(132) Venkatesh, R.; Marlow, W. H.; Lucchese, R. R.; Schulte, J. *J. Chem. Phys.* **1996**, *104*, 9016.
(133) Brady, J. W.; Doll, J. D.; Thompson, D. L. J. *Chem. Phys.* **1981**, *74*, 1026.
(134) Murad, S.; Law, C. K. *Mol. Phys.* **1999**, *96*, 81.
(135) Ming, L.; Marković, N.; Svanberg, M.; Pettersson, J. B. C. *J. Phys. Chem. A* **1997**, *101*, 4011.
(136) Martynyuk, M. M. *Sov. Phys. Tech. Phys.* **1976**, *21*, 430.
(137) Martynyuk, M. M.; Tamanga, P. A. *Russ. J. Phys. Chem.* **2000**, *74*, 1045.
(138) Kelly, R.; Miotello, A. *Appl. Surf. Sci.* **1996**, *96*−*98*, 205.
(139) Miotello, A.; Kelly, R. *Appl. Phys. A* **1999**, *69*, S67.
(140) Kelly, R.; Miotello, A. *J. Appl. Phys.* **2000**, *87*, 3177.
(141) Sunner, J.; Ikonomou, M. G.; Kebarle, P. *Int. J. Mass Spectrom.* **1988**, *82*, 221.
(142) Song, K. H.; Xu, X. *Appl. Surf. Sci.* **1998**, *127*−*129*, 111.
(143) Yoo, J. H.; Jeong, S. H.; Mao, X. L.; Greif, R.; Russo, R. E. *Appl. Phys. Lett.* **2000**, *76*, 783.
(144) Bulgakova, N. M.; Bulgakov, A. V. *Appl. Phys. A* **2001**, *73*, 199.
(145) Hankin, S. M.; John, P. *J. Phys. Chem. B* **1999**, *103*, 4566.
(146) Fournier, I.; Brunot, A.; Tabet, J. C.; Bolbach, G. *Int. J. Mass Spectrom.* **2002**, *213*, 203.
(147) Karas, M.; Bahr, U.; Hillenkamp, F. *Int. J. Mass Spectrom.* **1989**, *92*, 231.
(148) Karas, M.; Glückmann, M.; Schäfer, J. *J. Mass Spectrom.* **2000**, *35*, 1.
(149) Karbach, V.; Knochenmuss, R. *Rapid Commun. Mass Spectrom.* **1998**, *12*, 968.
(150) Shiea, J.; Sunner, J. In ref 2, p 147.
(151) Wang, J.; Li, J.; Yip, S.; Wolf, D.; Phillpot, S. *Physica A* **1997**, *240*, 396.
(152) Meyers, M. A.; Aimone, C. T. *Prog. Mater. Sci.* **1983**, *28*, 1.
(153) Belak, J. *J. Comput.-Aided Mater.* **1998**, *5*, 193.
(154) Strachan, A.; Çağin, T.; Goddard, W. A. *Phys. Rev. B* **2001**, *63*, 060103.
(155) Oraevsky, A. A.; Esenaliev, R.; Jacques, S. L.; Tittel, F. K. *Proc. SPIE* **1995**, *2391*, 300.
(156) Paltauf, G.; Dyer, P. Review of photomechanical ablation mechanisms in this issue of *Chemical Reviews*.
(157) Hare, E.; Franken, J.; Dlott, D. D. *J. Appl. Phys.* **1995**, *77*, 5950.
(158) Venugopalan, V. *Proc. SPIE* **1995**, *2391*, 184.
(159) Itzkan, I.; Albagli, D.; Dark, M. L.; Perelman, L. T.; von Rosenberg, C.; Feld M. S. *Proc. Natl. Acad. Sci. U.S.A.* **1995**, *92*, 1960.
(160) Perelman, L. T.; Albagli, D.; Dark, M.; von Rosenberg, C.; Itzkan, I.; Feld M. S.; Schaffer, J. *Proc. SPIE* **1995**, *2391*, 316.
(161) Itzkan, I.; Albagli, D.; Banish, B. J.; Dark, M. L.; von Rosenberg, C.; Perelman, L. T.; Janes, G. S.; Feld M. S. *AIP Conf. Proc.* **1994**, *288*, 491.
(162) Hatanaka, K.; Kawao, M.; Tsuboi, Y.; Fukumura, H. *J. Appl. Phys.* **1997**, *82*, 5799.
(163) Leisner, A.; Röhling, U.; Dreisewerd, K.; Hillenkamp, F., private communication.
(164) Kelly, R.; Miotello, A. *Phys. Rev. E* **1999**, *60*, 2616.
(165) For complex materials, such as soft tissues, the time of mechanical equilibration can be significantly longer than the one predicted by this simple acoustic approximation, see refs 158 and 161.
(166) Jacques, S. L.; Oraevsky, A. A.; Thompson, R.; Gerstman, B. S. *Proc. SPIE* **1994**, *2134A*, 54.
(167) Kelly, M. W.; Lin, C. P. *Proc. SPIE* **1997**, *2975*, 174.
(168) Zhigilei, L. V.; Garrison, B. J. *Appl. Surf. Sci.* **1998**, *127*−*129*, 142.
(169) Sun, J. M.; Gerstman, B. S. *Phys. Rev. E* **1999**, *59*, 5772.
(170) Huth-Fehre T.; Becker, C. H. *Rapid Commun. Mass Spectrom.* **1991**, *5*, 378.
(171) Beavis, R. C.; Chait, B. T. *Chem. Phys. Lett.* **1991**, *181*, 479.
(172) Pan, Y.; Cotter, R. J. *Org. Mass Spectrom.* **1992**, *27*, 3.
(173) Sibold D.; Urbassek, H. M. *Phys. Rev. A* **1991**, *43*, 6722.
(174) Kelly, R. *J. Chem. Phys.* **1990**, *92*, 5047.
(175) Landau, L. D. and Lifshitz, E. M. Fluid Mechanics, Pergamon: New York, 1987.

CR010459R